Assessment of Improved Ross–Li BRDF Models Emphasizing Albedo Estimates at Large Solar Angles Using POLDER Data

Yaxuan Chang, Ziti Jiao, Xiaoning Zhang, Linlu Mei, Yadong Dong, Siyang Yin, Lei Cui, Anxin Ding, Jing Guo, *Member, IEEE*, Rui Xie, Zidong Zhu, and Sijie Li

***Abstract*— Surface albedo is closely related to the Earth's energy budget and is usually estimated by integrating remotely sensed bidirectional reflectance distribution function (BRDF) data based on the widely used Ross–Li kernel-driven models. However, for large solar zenith angles (i.e., SZAs > 70°), albedo estimation using the operational algorithm of the Moderate Resolution Imaging Spectroradiometer (MODIS), i.e., RossThick-LiSparseReciprocal (RTLSR), is not recommended because it is reported to somewhat underestimate the black-sky albedo (BSA) at large SZAs based on ground albedo measurements. Recently, various combinations of the Ross–Li BRDF models with improved capabilities have been developed, and the assessments of these models based on worldwide satellite BRDF data with good spatial sampling, particularly at the large view and solar angles, will be important to improve an understanding of their performance in estimating intrinsic albedos. Following previous studies, the objective of this study is to further assess a series of hotspot-corrected Ross–Li models by demonstrating their ability to fit the POLarization and Directionality of the Earth's Reflectances (POLDER) data sets and estimate albedo, especially at large SZAs, based on selected concurrent POLDER and MODIS data. The hotspot-corrected RTLSR model obtained by combining the RossThickChen and LiSparseReciprocalChen kernels (RTLSR_C) shows the best fitting ability, with a high cumulative frequency of small root-mean-square errors (RMSEs), thus confirming previous conclusions. Model differences mainly appear in albedo estimates, especially BSA estimates at large SZAs. The BSAs estimated by other models are significantly different from the RTLSR_C estimates in the near-infrared (NIR) and red bands as the SZA increases to approximately 60° and 70°, respectively. In this case, RossThinChen-LiSparseReciprocalChen (RTNLSR_C) yields higher BSA estimates than those of RTLSR_C. Comparisons of the MODIS and POLDER albedos estimated with Ross–Li models show that models with the RossThinChen kernel yield higher BSA estimates than those of the RTLSR_C model as the SZA increases. The results indicate that the retrieved albedo is likely to be more accurate with appropriately selected kernels for BRDF models at large SZAs, providing guidance for selecting suitable combinations of multiple kernels.**

***Index Terms*— Albedo, bidirectional reflectance distribution function (BRDF), moderate resolution imaging spectroradiometer (MODIS), POLarization and directionality of the Earth's reflectances (POLDER), Ross–Li models.**

Manuscript received March 17, 2020; revised July 17, 2020 and October 1, 2020; accepted October 7, 2020. This work was supported in part by the National Key Research and Development Program of China under Grant 2017YFA0603001 and in part by the National Science Foundation of China under Grant 41971288. *(Corresponding author: Ziti Jiao.)*

Yaxuan Chang is with the State Key Laboratory of Remote Sensing Science, Jointly Sponsored by Beijing Normal University and Institute of Remote Sensing and Digital Earth, Chinese Academy of Sciences, Beijing 100875, China, also with the Beijing Engineering Research Center for Global Land Remote Sensing Products, Faculty of Geographical Science, Institute of Remote Sensing Science and Engineering, Beijing Normal University, Beijing 100875, China, and also with Tianjin Municipal Bureau of Planning and Natural Resources, Tianjin 300143, China.

Ziti Jiao, Xiaoning Zhang, Siyang Yin, Lei Cui, Anxin Ding, Jing Guo, Rui Xie, Zidong Zhu, and Sijie Li are with the State Key Laboratory of Remote Sensing Science, Jointly Sponsored by Beijing Normal University and Institute of Remote Sensing and Digital Earth, Chinese Academy of Sciences, Beijing 100875, China, and also with the Beijing Engineering Research Center for Global Land Remote Sensing Products, Faculty of Geographical Science, Institute of Remote Sensing Science and Engineering, Beijing Normal University, Beijing 100875, China (e-mail: jiaozt@bnu.edu.cn).

Linlu Mei is with the Institute of Environmental Physics, University of Bremen, 28359 Bremen, Germany.

Yadong Dong is with the State Key Laboratory of Remote Sensing Science, Jointly Sponsored by Institute of Remote Sensing and Digital Earth, Chinese Academy of Sciences and Beijing Normal University, Beijing 100875, China.

Color versions of one or more figures in this article are available at https://doi.org/10.1109/TGRS.2020.3030948.

Digital Object Identifier 10.1109/TGRS.2020.3030948

I. Introduction

LAND surface albedo, defined as the ratio of the reflected over the incoming solar flux [1], has long been recognized as an important energetic parameter related to the radiative properties of the land surface. Albedo is related to directional reflectance, which is usually described by the bidirectional reflectance distribution function (BRDF); this function represents the inherent reflectance anisotropy of the land surface and characterizes the directional reflectance in terms of its spectral, angular, spatial, and temporal properties [2]. The BRDF physically based models can explain the main causes of anisotropic reflectance and the corresponding nonlinear relationship with the albedo [3], and they permit calculation of the land surface albedo [4]–[7]. Both the BRDF and albedo are influenced by land surface properties, such as the surface structure and optical characteristics. In climate studies, albedo data sets are usually required to satisfy an absolute accuracy of 0.02–0.05; the required measurement uncertainty of albedo from the Global Climate Observing System (GCOS) exhibits a maximum of (5%; 0.0025); and the stability exhibits a maximum of (1%; 0.001) [8], which is essential for some climate

models [9]. Such models are utilized to evaluate the impact of human activities on climate change [10]. Therefore, the high-accuracy estimation of the BRDF and albedo, particularly on the global scale, is essential not only for climate change but also for weather forecasts, retrievals of various parameters and vegetation indicators, such as the clumping index (CI), a fraction of absorbed photosynthetically active radiation (FAPAR), and normalized difference vegetation index (NDVI), and environment-related studies [11].

Methods of estimating surface albedo based on satellite remote sensing observations can be divided into two categories. Methods in the first category rely on the parameter optimization of a kernel-driven BRDF model on a set of sufficient multiangular observations, and the albedo is obtained by hemispherical geometrical integration of the BRDF function itself. One example is the full inversion algorithm used to generate the Moderate Resolution Imaging Spectroradiometer (MODIS) albedo products that are obtained via the direct integration of BRDF measurements through the use of the RossThick-LiSparseReciprocal (RTLSR) model. By contrast, for cases in which the available multiangular observations are insufficient for performing full model inversion, prior knowledge regarding the anisotropic reflectance of the land surface must be used to estimate the surface albedo [12]. Various methods have been designed that use prior knowledge of the surface BRDF for albedo estimation. These methods include algorithms developed to consider major global vegetation types [13]–[15] and algorithms that use the NDVI [16], [17]. Recently, the BRDF archetypal method has been developed and evaluated as a means of using prior knowledge in the estimation of surface albedos [18]–[20] based on a hotspot-corrected BRDF model [21]. A direct albedo estimation approach has been developed based on and adapted to various operational instruments [22]–[26]. This method is mainly based on a reflectance lookup table (LUT), with the aim of performing a regression between the top of the atmosphere (TOA) spectral reflectance and the surface albedo for corresponding angular geometries. All these methods offer a better understanding of how prior knowledge of surface BRDFs can be used to improve the accuracy of land surface albedo estimates.

The accuracy of albedo estimation is related to the choice of the BRDF model because different models tend to have slightly different abilities to characterize certain typical BRDF features, particularly the reflectances at large solar zenith angles (SZAs) and/or in the hotspot direction, where the view and illumination angles coincide, even when observations with reasonably wide angular sampling are available. Currently, semiempirical models or physically based kernel-driven models, such as the Rahman–Pinty–Verstraete (RPV) model [27] or RTLSR [5], are widely used to estimate surface BRDFs and albedos. In particular, the available semiempirical linear kernel-driven models include different forms of geometric-optical (GO) kernels and volumetric scattering kernels that have been developed for various purposes. Among them, the RTLSR model has been adopted as the operational algorithm used to produce the MODIS BRDF/albedo product suite. Originally, a kernel-driven model with the RossThick (RT) kernel as the volumetric scattering kernel and the Roujean kernel as the GO kernel was proposed by Roujean *et al.* [28]. Subsequently, the RossThin (RTN) kernel was developed as a volumetric scattering kernel to represent the case of a small leaf area index (LAI), and various other GO kernels were developed, including LiSparse (LS), LiDense (LD), and LiTransit (LT) [29], [30]. To improve the performance of kernel-driven BRDF models in various remote sensing applications, particularly for retrieving the vegetation CI [31]–[33], various attempts have been made to correct for the hotspot effect in such models, especially the default MODIS RTLSR model [21], [34]–[37]. Kernel-driven models have been validated through early direct assessments of model performance [38], [39] and through major assessments of routine remote sensing products that are currently being generated [40]–[44]. Most recently, a snow kernel has been developed and assessed to better model the anisotropic reflectance of pure snow in a kernel-driven BRDF model framework [45]–[47]. The improved model has been implemented in SCIATRAN [48] and used for the retrieval of aerosol optical thickness over snow [49]. All these efforts have provided further insight into kernel-driven BRDF models and support various potential applications in the remote sensing community.

Despite these efforts, different kernels were designed for different scenarios and purposes, e.g., the Ross kernels to characterize thin and dense forests or Li kernels to describe various sparse vegetation canopies, so that a comprehensive assessment of this series of models and the applications for which they are suited is still advisable.

The POLarization and Directionality of the Earth's Reflectances (POLDER) provides, at the global scale, high-quality BRDF archive data sets with good geometrical sampling, including data for view zenith angles (VZAs) greater than 60°, where the range of its viewing azimuth angle covers almost any azimuthal direction (i.e., 0°–360°), and for geometries exhibiting the hotspot effect. However, most current satellite sensors rarely offer such capabilities. Notably, the general accuracy statement for MODIS albedo products declares that data with SZAs greater than 70° should be considered suspect (https://modis-land.gsfc.nasa.gov/ValStatus.php?ProductID=MOD43), consistent with previous reports that the MODIS RTLSR algorithm likely underestimates the albedo at large SZAs [41]. Moreover, further development of hotspot-corrected models will require a comprehensive assessment of these models using a set of observations with good spatial sampling on the global scale, such as the POLDER data, although it must be acknowledged that the POLDER data have a relatively coarse spatial resolution and, thus, capture less spatial variability in the surface reflectance than the MODIS data [42], [50]. In previous similar model performance evaluation studies, the multiangular data sets used were mainly obtained via ground measurements and included only a limited small range of SZAs [38], [39]. Further assessment of these improved models in terms of BRDF/albedo estimation, especially with a focus on the performance at large SZAs, will be helpful for potential applications in polar areas and mid-latitude areas in the winter season.

Previous studies regarding field measurements and validations show that albedo increases with SZA over different surface types, including snow, desert, vegetated, and ocean surfaces [40], [41], [51]–[53]. Even along the same geographic latitude, SZA also changes from sunrise to sunset, which causes the albedo fluctuations. Satellite albedo estimation products provide a global scale albedo by using various radiative transfer models considering different SZA and VZA variations [54]. However, the operational MODIS BRDF/Albedo algorithm was reported to probably cause an albedo bias at large SZAs ($>70°$) by the MODIS BRDF/Albedo product team that evaluated MODIS albedo products using field measurements and showed that the magnitudes of negative bias increase to 0.07 at the SZA $> 65°$. Recently, a commentary on MODIS snow albedo bias at high SZAs relative to theory and to *in situ* observations in Greenland [55] emphasized the importance of making appropriate use of the extensive quality flags available with the MODIS BRDF/Albedo. Most recently, the development of a snow kernel to better model the anisotropic reflectance of pure snow in a kernel-driven BRDF model framework concludes that such a snow kernel development has the potential to improve snow albedo estimation at large SZAs [45], [47]. All these efforts underline the importance of an accurate estimation of albedo at large SZAs in different scales and in theory, based on the kernel-driven BRDF model.

In this article, we present a comprehensive assessment of the improved Ross–Li model series in regard to BRDF/albedo retrieval by using POLDER BRDF data sets. The main purpose of this assessment is to investigate whether different Ross–Li model combinations may offer significant improvements in albedo estimation relative to the RTLSR model, particularly at large SZAs. First, we evaluate the fitting abilities of hotspot-corrected Ross–Li models by using the root-mean-square error (RMSE) as the evaluation metric. Second, we evaluate the hotspot impact on albedo estimation. Third, we compare black-sky albedo (BSA) estimations of hotspot-corrected models with the corresponding MODIS algorithm BSA estimations. Finally, we indirectly apply the RTNLSR_C model in conjunction with MODIS data to estimate albedo and compare it with site observation data and MODIS albedo products.

II. Data

A. POLDER Data Sets

The POLDER sensor was carried on the Polarization & Anisotropy of Reflectances for Atmospheric Sciences coupled with Observations from a Lidar (PARASOL) platform, which was launched by the National Centre for Space Studies (CNES) in 2004. The spatial resolution of POLDER was approximately 6 km $\times$ 7 km at nadir, and the maximum field of view (FOV) was 114° [56]. Affected by the curvature of the Earth, the VZAs along and cross track were $\pm 61°$ and $\pm 50°$, respectively. As the satellite flew over a target, at most 16 observations of the target are in different geometric configurations for each revisiting time [57]. These observations provide a broad sampling of BRDF values for VZAs of up to almost 70° and SZAs of up to 75°, assuming stability of the target [56]. Importantly, hotspot ($\Delta\varphi = 0$) signatures are also included in many individual samples.

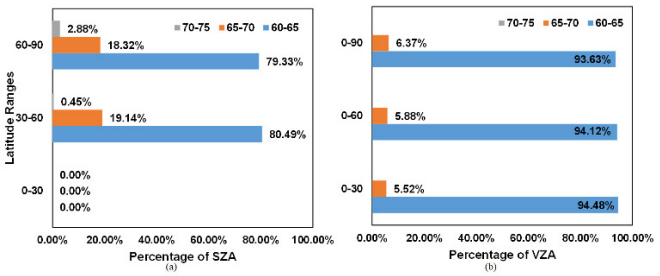

Fig. 1. Cumulative bar plots presenting the proportions of observations at large SZAs and VZAs considering the latitude. A large angle is defined as an angle larger than 60° in the POLDER data sets. (a) SZA distribution. (b) VZA distribution. The blue, orange, and gray bars represent three angular intervals of [60°, 65°), [65°, 70°), and [70°, 75°], respectively. The latitude ranges are [0°, 30°), [30°, 60°), and [60°, 90°].

Two POLDER data sets, which provide multiangular data for the years of 2005 to 2006 [58] and 2008 [57], were collected and used in this research. In general, these two data sets provide sufficient observations in various observation geometries, especially in the backscatter direction in which the hotspot effect occurs, and they have been used as prior knowledge to estimate several important physical parameters of vegetation, e.g., the CI [31]–[33], [59] and canopy height [60]. Notably, all the POLDER data used here mainly correspond to a single International Geosphere-Biosphere Programme (IGBP) land cover type, and no records are available regarding the effects of aerosols and clouds [56]. In this study, we make use of six spectral bands with central wavelengths of 490, 565, 670, 765, 865, and 1020 nm, where the bandwidths of these spectral bands are 16.5, 15.5, 15.0, 38.0, 33.5, and 17.0 nm, respectively. A simple statistical analysis of the angular distributions of the selected data depending on latitude reveals that, in the middle and high latitude, the SZA ranges 0° to 75°, and the VZA ranges 0° to 70° in all latitude ranges. More detailed statistics on the distributions of the large zenith angles are shown in Fig. 1, which illustrates the percentages corresponding to three ranges of relatively large zenith angles ($>60°$) for both the view and solar geometries in the low-, middle-, and high-latitude ranges. With the increase in the latitude, the percentage of SZA ranging from 70° to 75° in all relatively large zenith angles reaches 2.88%, which provides sufficient observations under large SZAs.

Unsurprisingly, the large-VZA data account for a relatively small proportion of the POLDER data used here because it is still challenging for satellite sensors to acquire large-VZA observations. Fortunately, although the POLDER data do not include VZAs greater than 70°, these data are nevertheless likely to provide the necessary constraints for kernel-driven BRDF models in the large-VZA range, particularly relative to other satellite sensors, e.g., MODIS, which has been reported to have a typical approximate range of VZA $< 55°$ [41].

B. MODIS Products

To assess the directional hemisphere, also known as BSA [61], with estimates obtained from the POLDER data

set under the constraints of large VZAs using the improved Ross–Li models, we selected the MCD43A1 MODIS BRDF product to calculate the corresponding BSAs for comparison. The RTLSR model is currently utilized as the operational algorithm for MODIS. The three BRDF model parameters, isotropic ($f_{\rm iso}$), geometrical ($f_{\rm geo}$), and volumetric ($f_{\rm vol}$) model parameters, provide the best-fit and well-sampled values from the RTLSR model inversion [62] that can be used to easily calculate the BSA in any solar geometry. We also chose several other MODIS products to select relatively pure coarse-spatial-resolution POLDER pixels. The quality flag QA = 0 in the MCD43A2 BRDF product was first applied to select the best-quality BRDF parameters [62], [63]. The official IGBP land cover product MCD12Q1 [64] was used to select pixels with relatively pure snow-free land cover from among the coarse POLDER pixels. The official vegetation continuous fields (VCFs) product MOD44B [65], which represents the percentage of one specific land cover type (vegetation, herbaceous, or bare ground) within a MODIS pixel, were further used as a constraint to select the most homogeneous area at POLDER spatial resolution.

The 500-m resolution MODIS BRDF parameters with the best QA (i.e., QA = 0) were averaged to generate a coarse MODIS BRDF data set with a spatial resolution of ~6.5 km × 6.5 km, given the assumption that linear BRDF models can effectively model surface heterogeneities [42], [50]. The averages were performed over an array of 13 × 13 pixels of the 500-m MODIS MCD43A1, which roughly corresponds to match the size of a single POLDER pixel (6 km × 7 km) [50]. Notably, in the process of selecting the relatively pure POLDER data, we used 13 × 13 arrays of pixels of the same land cover type from the 500-m MODIS IGBP land cover product, where each array corresponded to a coarse POLDER pixel. As a further layer of constraint, the VCF product was used to ensure specific values of at least 60% for tree and nontree vegetation and at least 90% for bare ground [50]. With all these constraints mentioned above, we finally obtained 1815 pixels of POLDER BRDF data and the corresponding 13 × 13 × 1815 pixels of MODIS BRDF data in both the red and near-infrared (NIR) bands.

C. Albedo Observation Data

We selected eight site observations from 47 sites, which includes albedo observations, MODIS kernel parameters, and corresponding angle information. These eight observations are observed at SZA = 30°, 45°, 60°, and 75°, respectively, and exhibit good homogeneity that indicates effective representativeness for the MODIS pixels covering these ground sites. For more details about these *in situ* albedo measurements, please refer to the previous research by Zhang *et al.* [26].

III. Method

A. Hotspot-Corrected Kernel-Driven Ross–Li BRDF Models

The linear, semiempirical, kernel-driven BRDF model originally derived by Roujean *et al.* [28] is expressed as a linear combination of isotropic, volumetric, and GO scattering kernels [29], [66]. The spectral anisotropic reflectance is given as follows:

$$R(\theta_i,\theta_v,\varphi,\lambda) = f_{\rm iso}(\lambda) + f_{\rm vol}(\lambda)K_{\rm vol}(\theta_i,\theta_v,\varphi) + f_{\rm geo}(\lambda)K_{\rm geo}(\theta_i,\theta_v,\varphi) \quad (1)$$

where $R(\theta_i, \theta_v, \varphi, \lambda)$ is the surface anisotropic reflectance in waveband λ in the angular geometry represented by SZA (θ_i), view zenith angle (θ_v), and relative azimuth angle (φ). $K_{\rm vol}(\theta_i, \theta_v, \varphi)$ and $K_{\rm geo}(\theta_i, \theta_v, \varphi)$ represent the volumetric and the GO scattering kernel, respectively, which are expressed in terms of θ_i, θ_v, and φ between the incident and reflecting directions. The isotropic scattering kernel has a constant value (i.e., 1.0). $f_{\rm iso}$, $f_{\rm vol}$, and $f_{\rm geo}$ are spectrally dependent coefficients, which represent the weights of the corresponding scattering kernels and need to be retrieved. $f_{\rm iso}$ represents the isotropic spectral reflectance for coincident illumination and viewing direction at nadir. $f_{\rm vol}$ and $f_{\rm geo}$ characterize the anisotropic reflectance of a non-Lambertian reflective surface.

$K_{\rm geo}$ characterizes the shadow effects of a canopy [67], and $K_{\rm vol}$ represents the volumetric scattering effects of a canopy of randomly distributed leaves in the single-scattering approximation [68]. The RT kernel ($K_{\rm RT}$) and the LiSparseReciprocal (LSR) kernel ($K_{\rm LSR}$) are adopted in the MODIS BRDF/albedo operational algorithm. However, with these two kernels, the hotspot signature cannot be explicitly formalized. To address this problem, Jiao *et al.* [21] applied a hotspot function with an exponential form to the volumetric scattering kernel to obtain the hotspot-corrected RossThickChen (RTC) kernel ($K_{\rm RTC}$). We follow the same method to correct the RTN kernel to obtain the RossThinChen (RTNC) kernel. The hotspot-corrected RTC and RTNC volumetric scattering kernels are shown in (2) and (3)

$$K_{\rm RTC} = \frac{(\pi/2-\xi)\cos\xi+\sin\xi}{\cos\theta_v+\cos\theta_i}\times\left(1+C1e^{-\frac{\xi}{C2}}\right)-\frac{\pi}{4} \quad (2)$$

$$K_{\rm RTNC} = \frac{(\pi/2-\xi)\cos\xi+\sin\xi}{\cos\theta_v\times\cos\theta_i}\times\left(1+C1e^{-\frac{\xi}{C2}}\right)-\frac{\pi}{2} \quad (3)$$

$$\cos\xi = \cos\theta_i\cos\theta_v+\sin\theta_i\sin\theta_v\cos\varphi \quad (4)$$

where ξ is the phase angle and is defined in (4). The term $1+C_1\exp(-\xi/C_2)$ is the so-called hotspot function, where C_1 and C_2 are two adjustable hotspot parameters that modify the height and width of the original shape of the volumetric scattering kernel. This hotspot function was previously suggested by Chen and Cihlar [35] to represent a simplified version of the hotspot effect in the four-scale model.

However, some slight underestimation also exists in the RossThickChen-LiSparseReciprocal (RTCLSR) model, particularly in the rare case in which the volumetric contribution to the reflectance anisotropy is null ($f_{\rm vol} = 0$). In this case, the corrected volumetric scattering kernel no longer plays a role. To address this problem, Dong *et al.* [69] proposed a method in which the above exponential hotspot function is also applied to the overlap function of the LSR kernel to improve the simulation capability of $K_{\rm LSR}$. This improved kernel, called LiSparseReciprocalChen (LSRC), is shown as follows:

$$K_{\rm LSRC} = O\left(\theta_i',\theta_v',t\right)\left(1+C1e^{-\frac{\xi}{C2}}\right)-\sec\theta_i'-\sec\theta_v' + \frac{1}{2}\left(1+\cos\xi'\right)\sec\theta_v'\sec\theta_i' \quad (5)$$

where the function O is the overlap between the viewing and illumination shadows, which theoretically determines the hotspot effect for a discrete vegetation canopy at the crown scale [67]. This improvement in the overlap function can enhance the hotspot effect because of the further consideration of the leaf distribution within the canopy

$$O\left(\theta_i', \theta_v', t\right) = \frac{1}{\pi}(t - \sin t \cdot \cos t)\left(\sec\theta_i' + \sec\theta_v'\right) \tag{6}$$

in which the variables are defined as follows:

$$\cos t = \frac{h}{b}\frac{\sqrt{D^2\left(\tan\theta_i' \tan\theta_v' \sin\varphi\right)}}{\sec\theta_i' + \sec\theta_v'} \tag{7}$$

$$D = \sqrt{\tan^2\theta_i' + \tan^2\theta_v' - 2\tan\theta_i' \tan\theta_v' \cos\varphi} \tag{8}$$

$$\cos\xi' = \cos\theta_i' \cos\theta_v' + \sin\theta_i' \sin\theta_v' \cos\varphi \tag{9}$$

$$\theta_i' = \tan^{-1}\left(\frac{b}{r}\tan\theta_i\right) \quad \text{and} \tag{10}$$

$$\theta_v' = \tan^{-1}\left(\frac{b}{r}\tan\theta_v\right) \tag{11}$$

where h is the mean height from the center of the crown to the ground, and b and r are the mean vertical half-axis and mean horizontal radius, respectively, of the modeled ellipsoid crown. Therefore, h/b and b/r represent the shape and relative height, respectively, of the crown. In general, h/b and b/r are set to values of 2 and 1, respectively.

In this article, we also adopt the same improvement method to correct other GO kernels. The other GO kernels obtained after hotspot correction are referred to as LiTransitReciprocalChen (LTRC) and LiDenseReciprocalChen (LDRC) kernels. The corresponding GO kernels are defined as follows:

$$K_{\mathrm{LDRC}} = \frac{\left(1 + \cos\xi'\right)\sec\theta_v' \sec\theta_i'}{\sec\theta_i' + \sec\theta_v' - O\left(\theta_i', \theta_v', t\right)\left(1 + C1e^{-\frac{\xi}{C2}}\right)} - 2. \tag{12}$$

To improve the extrapolation ability of GO models, a kernel called LiTransitReciprocal (LTR) has been developed [30], [70]. This *kernel* takes a transitional form between the LiSparseReciprocal LSR and LiDenseReciprocal (LDR) kernels. If the critical value of B is greater than 2, which means that the multiangular data have large VZAs, then the LDRC kernel function should be applied in the model. Otherwise, LSRC should be used. Thus, the LTR kernel can be improved in the same way as LSR and LDR

$$K_{\mathrm{LTRC}} = \begin{cases} K_{\mathrm{LSRC}}, & B \le 2 \\ L_{\mathrm{LDRC}} = \dfrac{2}{B}K_{\mathrm{LSR}}, & B > 2 \end{cases} \tag{13}$$

where

$$B = \sec\theta_i' + \sec\theta_v' - O\left(\theta_i', \theta_v', \varphi\right). \tag{14}$$

By combining all the improved volumetric scattering kernels and GO kernels mentioned earlier, we can construct a new series of improved Ross–Li models (see Table I). RTC and RTNC are the abbreviations of RossThickChen and RossThinChen kernels, respectively. LSRC, LDRC, and LTRC are the abbreviations of LiSparseRChen, LiDenseRChen, and LiTransitRChen, respectively, where _C after the name of each model means that this model is modified by the hotspot correction function. Unlike the RTCLSR model, the models listed in Table I do not introduce new free hotspot parameters, thus simplifying their form and application for potential users [69].

TABLE I
IMPROVED ROSS–LI MODELS

Kvol \ Kgeo	LiSparseRChen	LiTransitRChen	LiDenseRChen
RossThickChen	RTLSR_C	RTLTR_C	RTLDR_C
RossThinChen	RTNLSR_C	RTNLTR_C	RTNLDR_C

The albedo is the angular integral of the BRDF. Based on these improved kernel-driven models, the POLDER data sets, and the optimal hotspot parameters, we can retrieve the three constrained kernel parameters (i.e., f_{iso}, f_{geo}, and f_{vol}) of the BRDF models and then easily simulate the surface reflectance in any angular geometry in the forward mode. The BSA (directional hemispherical reflectance) at typical SZAs ranging from 0° to 75° in 5° intervals and the white sky albedos (WSAs; bihemispherical) can then be calculated using these kernel parameters for all spectral bands through model integration. The functions for calculating the BSA and WSA are shown as follows:

$$\mathrm{BSA}(\theta_i, \lambda) = \frac{1}{\pi}\int_0^{2\pi}\int_0^{\frac{\pi}{2}} R(\theta_i, \theta_v, \varphi, \lambda)\sin\theta_v \cos\theta_v d\theta_v d\varphi \tag{15}$$

$$\mathrm{WSA}(\lambda) = 2\int_0^{\frac{\pi}{2}} \mathrm{BSA}\left(\theta_i, \lambda\right)\sin\theta_i \cos\theta_i d\theta_i \tag{16}$$

where θ_i, θ_v, φ, and λ are the same as in (1).

B. Anisotropic Flat Index for BRDF Classification

In this study, we adopt the AFX to capture the variability in the shape of the BRDF. The AFX is defined as the ratio of the WSA to the isotropic kernel parameter [71], which is a linear combination or a product of kernels. It combines all three parameters and the kernel values into a single variable. In addition, it eliminates the influence of spectral reflectance, thus making the BRDF "purer" and easier to compare among different bands. The function for calculating the AFX is shown as follows:

$$\mathrm{AFX} = 1 + \frac{f_{\mathrm{vol}}(\lambda)}{f_{\mathrm{iso}}(\lambda)} \times H_{\mathrm{vol}} + \frac{f_{\mathrm{geo}}(\lambda)}{f_{\mathrm{iso}}(\lambda)} \times H_{\mathrm{geo}} \tag{17}$$

where H_{vol} and H_{geo} are the bihemispherical integral values of the volumetric scattering kernel and the GO kernel, respectively. For a given scattering type, these integrals are constant.

The volumetric scattering kernels exhibit typical bowl shapes, while the GO kernels exhibit dome shapes. The shape of the BRDF varies from dome-like to bowl-like depending on the weight of each kernel. When these two scattering components precisely balance each other, the AFX value is 1.0, indicating a surface with Lambertian reflectance, and the curve of the BRDF is almost flat at the edge. When the volumetric scattering component plays the main role in scattering from the

land surface (i.e., AFX $>$ 1.0), a more bowl-shaped reflectance pattern will be exhibited. By contrast, an AFX value of $<$ 1.0 indicates that surface scattering is the dominant component; in this case, the BRDF curve will tend to be more dome-shaped.

Generally, we consider the red and NIR bands as the typical wavebands in which, to examine the model characteristics according to observations, multiangular data in the red band exhibit mainly dome-shaped anisotropy (AFX $<$ 1), whereas the data in the NIR band are more prone to bowl-shaped anisotropy (AFX $>$ 1).To identify clusters of AFX values in similar ranges, we calculated the AFX for each POLDER pixel in both the red and NIR bands. To obtain the most representative data, we select the bottom ten percent of the original POLDER data in the red band (i.e., AFX $<$ 0.707, lower 10% of 12 769 POLDER pixels) and the top 10% of the data in the NIR band (i.e., AFX $>$ 1.017, higher 10% of 13 377 POLDER pixels). These groups of data contain 1265 and 1334 data points. Based on these representative data, we further compare and analyze the hotspot effect for the improved Ross–Li models and the variability in the dome/bowl-shaped BRDFs and derived albedos.

C. Error Functions

The RMSE, which is commonly used as a quantitative criterion for the evaluation of kernel-driven models, is defined in (18)

$$\mathrm{RMSE} = \sqrt{\frac{\sum_{j=1}^{n}\left(R^{\mathrm{obs}} - R^{\mathrm{model}}\right)^2}{n-3}} \tag{18}$$

where R^{obs} is the observed reflectance, R^{model} is the reflectance simulated by the corresponding BRDF model, and n is the number of observations. To eliminate the impact of spectral differences on the BRDFs, we use the isotropic parameter of the model (i.e., f_{iso}) to normalize the RMSE values, thereby obtaining directly comparable RMSE_r values for different bands [32]. RMSE_r is calculated, as shown in (19). This method eliminates the differences in the BRDFs caused by spectral reflectance and, thus, emphasizes the variability of the "pure" BRDFs

$$\mathrm{RMSE\_}r = \sqrt{\frac{\sum_{j=1}^{n}\left(\frac{R^{\mathrm{obs}} - R^{\mathrm{model}}}{f_{\mathrm{iso}}}\right)^2}{n-3}}. \tag{19}$$

Linear inversion is not feasible for retrieving the three model parameters and two hotspot parameters simultaneously. We also use the RMSE method to determine the optimal hotspot parameters (C_1 and C_2) for the six improved models in six different bands based on the POLDER hotspot data. Theoretically, once the three model parameters are known and sufficient multiangular observations are available, the two hotspot parameters can be derived via nonlinear least-squares methods for each set of data. Moreover, the accuracy of the hotspot parameters is affected by the number of observations in the vicinity of the hotspot direction, i.e., $\xi \leq 5^\circ$ [21], [69], [72]. Thus, to maintain the linearity of these improved kernel-driven models to ensure user convenience and retrieval performances, one method is to determine the two hotspot parameters as internally constant prior values (similar to h/b and b/r in the GO kernel). In this study, we follow a method [21], [69] that consists of iteratively changing the values of C_1 and C_2 in small, fixed steps and then calculating the corresponding RMSE values. Finally, we can determine the optimal C_1 and C_2 by selecting the lowest RMSE among all calculated values. The steps of retrieving the two hotspot parameters are explained as follows (for the RTLSR_C model and a single band as an example).

First, we set the ranges of variation from 0.1 to 2.0 in a step of 0.1 for C_1 and from 1.0° to 10.0° in a step of 0.1 for C_2. We set the initial values of C_1 and C_2 in the RTLSR_C model to 0.1 and 1.0°, respectively, and fit this model to each group of POLDER data. Based on the inversion of the three parameters for each group of data, we select the observed and simulated data corresponding to phase angles $\xi \leq 5^\circ$ to perform the optimization around only the hotspot region.

Second, we calculate the RMSE for each pair of C_1 and C_2 parameters.

Third, 2000 RMSEs (for 20 values of C_1 and 100 values of C_2) were calculated based on (18).

Finally, C_1 and C_2 optimal values are obtained by minimizing the RMSE.

D. Validation of RTNLSR_C Using Albedo Observations

Since MODIS official products do not provide the original multiangle reflectances and it is not possible for us to acquire the same multiangle reflectance as the operational MODIS product suite does, we, therefore, link three parameters of the RTLSR model to the model parameters being explored in this article by using a statistical method.

First, we construct the linear regression relationship of model parameters between RTLSR_C and RTNLSR_C models based on the POLDER data set and, thus, derive model regression coefficients for each band of POLDER data. Second, we match POLDER bands with MODIS bands from the corresponding visible bands to NIR bands. Third, we use the regression model in the first step to acquire MODIS RTNLSR_C BRDF parameters from the operational MODIS BRDF parameters. Fourth, we simulate single band albedo by RTNLSR_C BRDF parameters taking the general percentage of the diffuse skylight (i.e., 20%) for the MODIS pixels in the flux tower (20) [73]. Fifth, we perform a narrowband-to-broadband albedo conversion by Liang's research [74]. The conversion formula is shown in (21)

$$\mathrm{albedo}_{\mathrm{simulate}} = 0.8 \times \mathrm{BSA}(\theta_S, \lambda) + 0.2 \times \mathrm{WSA}(\lambda) \tag{20}$$

$$\begin{aligned}\alpha^{\mathrm{MODIS}} &= 0.160\alpha_1 + 0.291\alpha_2 + 0.243\alpha_3 + 0.116\alpha_4 \\ &\quad + 0.112\alpha_5 + 0.081\alpha_7 - 0.0015\end{aligned} \tag{21}$$

in which α_{1-7} represent the albedos of 648-, 859-,466-, 554-, 1244-, 1631-, and 2119-nm bands, respectively. Finally, we compare albedo simulated by RTNLSR_C and operational MODIS albedo products (i.e., RTLSR model) with albedo observations.

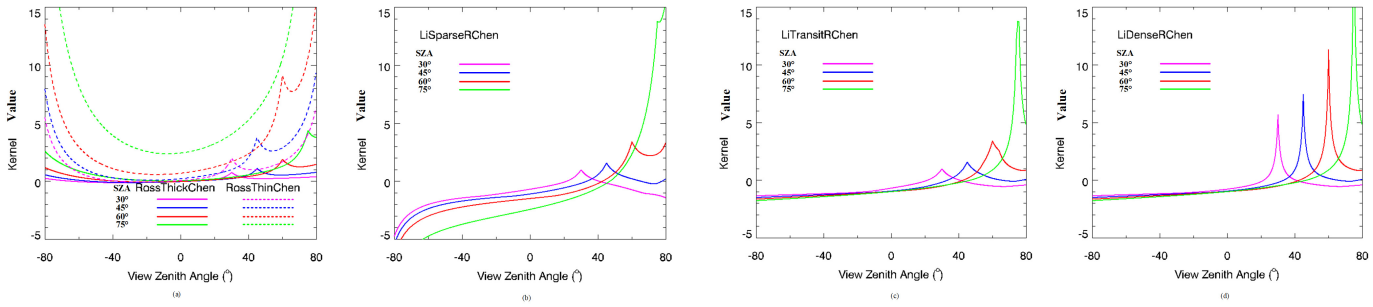

Fig. 2. Shapes of the kernels after hotspot correction with parameters of $C_1 = 0.7$ and $C_2 = 5.0$ at SZAs of 30°, 45°, 60°, and 75°. (a) Shapes of the two volumetric scattering kernels, with the dotted and solid lines representing RTNC and RTC, respectively. (b)–(d) LSRC, LTRC, and LDRC kernels, respectively.

E. Experimental Design

The design framework of this experiment is illustrated as follows.

Step 1: Preparatory processing, including data filtration and the determination of the optimal hotspot parameters. First, we use near-hotspot observations from the POLDER database corresponding to $\xi \leq 5°$ [21]. Then, we fit the six combined-kernel-driven models, with the two hotspot parameters (C_1 and C_2) as free parameters, to these selected POLDER BRDF data to calculate the simulated BRDFs. Next, we determine the optimal C_1 and C_2 values for each model in each band based on the lowest RMSE between the observed and simulated BRDFs. Finally, we apply these improved models with the corresponding optimal C_1 and C_2 values to all POLDER/BRDF data sets.

Step 2: Evaluation of the fitting abilities of hotspot-corrected models. Based on models and data in step 1, we calculate the RMSE and RMSE_r values to assess the fitting ability of models.

Step 3: The evaluation of the influence of hotspot correction on albedo estimation. To explore the ability of models to estimate albedo at large SZAs and the potential influence of the hotspot effect on the overall shape of the BRDF, data screened based on the AFX in the red and NIR bands are used to evaluate the influence of the hotspot parameters on the BSA estimates. Then, we identify the possible differences in the albedos, especially the BSAs at large SZAs that are derived by applying the six Ross–Li models to the POLDER data with sufficient multiangular observations. The significance of the differences between the other models and the MODIS operational algorithm, in particular, is examined by means of the t-test. Here, we use a nominal α value of 0.05 for the t-test to determine whether there is a significant difference in performance between the two models.

Step 4: Comparison between the improved models and the MODIS algorithm on BSA estimation. We select relatively pure 13×13 MODIS pixels and the concurrent POLDER pixels. The BSAs derived using the RTLSR_C model with the average MODIS BRDF parameters are used as the benchmark to compare the BSAs calculated using the six Ross–Li _C models based on the POLDER data against the corresponding average 6.5×6.5 km MODIS observations. This analysis will be helpful to identify potential problems identified in relation to the MODIS operational algorithm of MCD43A1, especially at large zenith angles.

Step 5: Validation of RTNLSR_C model using ground albedo observations. We follow the workflow in Section III-D to finish this validation. This validation helps to make the conclusion derived in step 4 more solid.

IV. Results and Analysis

A. Optimal Hotspot Parameters for the Six Improved Models

Models used here refer to Table I. The shapes of the hotspot-corrected kernels on the principal plane at four different SZAs are shown in Fig. 2. We can see that the RTNC kernel tends to have higher values around the hotspot than the RTC kernel, with more bowl-shaped BRDFs at large VZAs. The bowl shape of the BRDF in the case of the RTNC kernel is emphasized at higher SZAs as the SZA increases. The LTRC kernel has the same shape as the LSRC kernel around the hotspot, but its shape at large VZAs is the same as that of the LDRC kernel, representing the transition in shape from the LiSparseRChen to the LiDenseRChen kernel. In addition, as the SZA increases, the forward reflectance of the LiSparseRChen kernel rapidly decreases. With the same values of the hotspot parameters, the LDRC kernel appears more sensitive to these parameters. Based on the method introduced in Section II-B, we retrieved the optimal hotspot parameters for these six models in six different bands, as shown in Table II.

B. Examination of Model-Observation Fits for the Corrected Ross–Li Models

We first evaluate these BRDF models with the optimal fixed hotspot parameters (i.e., no free hotspot parameters) based on the fit-RMSEs obtained through comparison between POLDER real data and simulated data. The mean values of

TABLE II

THE OPTIMAL FIXED VALUES OF HOTSPOT PARAMETERS FOR THE VARIOUS COMBINED-KERNEL MODELS, AS CALIBRATED BASED ON THE SELECTED POLDER HOTSPOT DATA SET IN SIX DIFFERENT BANDS

Band		1	2	3	4	5	6
Model	λc^a	490	565	670	765	865	1020
RTLSR_C	C_1	0.4	0.5	0.5	0.4	0.5	0.4
	C_2	3.8	3.1	3.4	4.1	3.0	4.5
RTLTR_C	C_1	0.3	0.4	0.5	0.4	0.4	0.4
	C_2	2.6	1.8	1.3	1.6	1.5	1.6
RTLDR_C	C_1	0.2	0.2	0.2	0.2	0.2	0.2
	C_2	2.0	1.5	1.2	1.3	1.2	1.3
RTNLSR_C	C_1	0.6	0.6	0.7	0.6	0.6	0.6
	C_2	2.9	3.2	2.8	3.0	3.1	3.3
RTNLTR_C	C_1	0.5	0.5	0.6	0.5	0.5	0.5
	C_2	1.1	1.1	1.0	1.0	1.0	1.1
RTNLDR_C	C_1	0.2	0.2	0.2	0.2	0.2	0.2
	C_2	1.0	1.0	1.0	1.0	1.0	1.0

[a]λc is the central wavelength and the unit is nm. The unit of C_2 is in degrees.

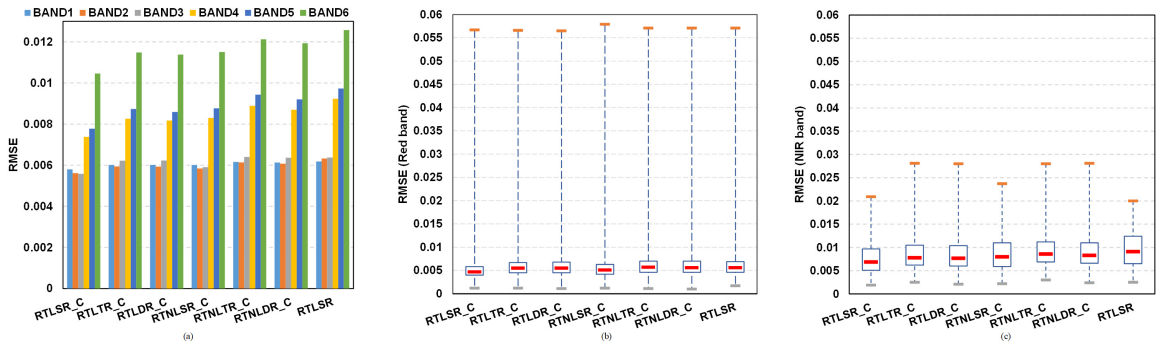

Fig. 3. (a) Mean values of the fit-RMSEs for the six combined-kernel models in six bands. (b) and (c) RMSE statistics in the red and NIR bands in boxplots, respectively. The orange and gray sticks represent the maximum and minimum values. The red sticks represent the median values.

the RMSEs for the six models in the six bands are shown in Fig. 3(a). The RMSE is the average value of RMSE computed over different POLDER pixels by each model in each band. In the visible wavebands, the discrepancies among the mean values of the fit-RMSEs in different bands are generally less than 0.001. The differences among the models are generally similar in the six bands. The RTLSR_C model, which is the MODIS operational algorithm with hotspot correction, shows the best fitting ability (i.e., the lowest RMSE). The models with the RTC volumetric scattering kernel have lower RMSEs than the models with the RTNC kernel when combined with the same GO kernel. One exception is that the RTNLSR_C model seems to show somewhat better fitting performance than the other models in which the RTNC kernel is used as the volumetric scattering kernel. For example, the mean RMSE values in the red and NIR bands for the RTNLSR_C model are 0.0059 and 0.0087, respectively; the values for the RTNLTR_C model are 0.0064 and 0.0094, respectively; and the values for the RTNLDR_C model are 0.0064 and 0.0092, respectively. Similar differences among these models were observed in the other bands.

Let us now consider the RMSE histograms calculated by the real and simulated POLDER data in the red and NIR bands; the results are shown in Fig. 3(b) and (c). Although the mean RMSEs in the NIR band are somewhat higher than those in the red band, they are generally less than 0.01, indicating that all models generally achieve good fits on the entire POLDER data archive. The differences between the maximum and minimum RMSE values in these two bands are not at the same level; especially, the difference in the red band is almost twice the difference in the NIR band, indicating that the uncertainty in these POLDER observations is definitely less in the NIR band than in the red band.

To evaluate the performance of the six improved combined-kernel BRDF models, both the RMSE and RMSE_*r* values are further examined. Fig. 4 illustrates the cumulative frequencies of the RMSE and RMSE_*r* values in the red and NIR bands.

Fig. 4 shows that all investigated models can fit the entire archive of the POLDER observations with high quality yielding quite low RMSE values in both the red and NIR bands although there are also some differences among the six models. All the hotspot-corrected models have better fitting abilities than the MODIS RTLSR model since the RMSE/RMSE_*r* cumulative distribution function of the RTLSR model increases slower than other models. In general, the RMSEs in the NIR band are significantly higher than those in the red band because the reflectance in the NIR band is

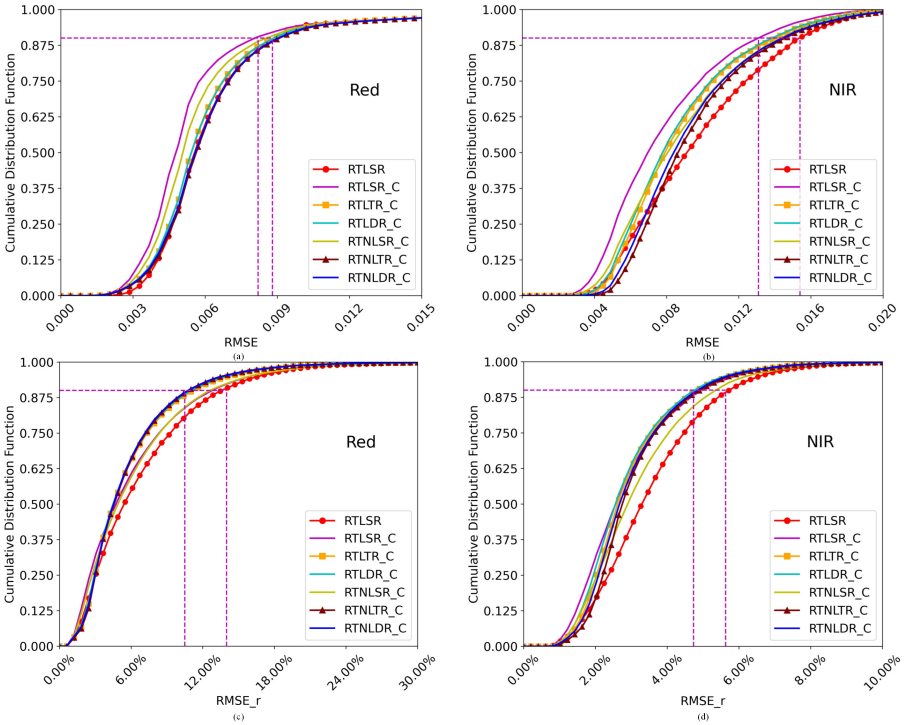

Fig. 4. Cumulative frequencies of the RMSE and RMSE_*r* values obtained when fitting all POLDER observations from both data sets and simulating the BRDFs using the six hotspot-corrected BRDF models with the optimal fixed hotspot parameter values (see Table I). (a) and (b) Cumulative frequencies of RMSE values of the red and NIR bands, respectively. (c) and (d) Cumulative frequencies of RMSE_*r* values of the red and NIR bands, respectively.

always higher than that in the red band for measurements that include various vegetation types. This is true for all models considered here. More than 90% of the POLDER observations have fit-RMSEs of less than 0.009 and 0.015 in the red and NIR bands, respectively. The cumulative frequencies of the fit-RMSEs for the RTLSR_C model increase more rapidly at low RMSE values than those for the other models in both bands, reaching approximately 90% at values of 0.0075 and 0.0125 in the red and NIR bands, respectively, which corresponds to the result in Fig. 3 and the good performance of the MODIS operational algorithm in previous studies. These findings indicate that the operational MODIS model with the hotspot-corrected kernels exhibits a stronger fitting ability than the other models. Among these models, the RTNLTR_C model shows a relatively slow increase in the cumulative frequencies of the fit-RMSEs in both bands, particularly in the NIR band. In the red band, the cumulative frequencies of the fit-RMSEs for the RTLTR_C and RTLDR_C models are almost the same, as are those for the RTNLTR_C and RTNLDR_C models, indicating that the models that include either the LDRC or LTRC kernel have a similar ability to fit the POLDER observations.

Once the different spectral influences caused by f_{iso} have been removed, the cumulative frequency results for RMSE_*r* indicate smaller differences in the fitting ability for these different models, particularly between the red and NIR bands, since the spectral differences are normalized out with respect to the corresponding spectral magnitudes, i.e., f_{iso}. The six models all reach cumulative frequencies of 90% at RMSE_*r* values ranging from 10.5% to 13.5% in the red band and from 4.5% to 5.5% in the NIR band. These results confirm the previous finding that the POLDER data in the NIR band have less uncertainty than those in the red band, most likely because of the weaker effects of the atmosphere and aerosols [57], [75]. With the exception of the RTLSR_C and RTNLSR_C models, the cumulative frequencies of the various models do not appear to exhibit significant differences [see Fig. 4(b)]. The RMSE_*r* analysis indicates that the RTLSR_C model does not always achieve the best performance in fitting all observations, even in the NIR band. Moreover, the RTNLSR_C model shows a distinctly poorer fitting ability, particularly with regard to RMSE_*r* values in the range of 2.5%–5.5% relative to the other models. This analysis of RMSE_*r* indicates that a comprehensive evaluation of these models based on the entire archive of POLDER observations can provide an improved understanding of the suitability of different models for different applications, allowing potential users to select appropriate models for their needs instead of completely relying on the RTLSR_C (or RTLSR) model. Therefore, in Sections IV-D to F, we will mainly focus on exploring the differences between RTLSR_C and the other models, especially for the case of albedo estimation at large SZAs.

C. Influence of Hotspot Correction on Albedo Estimation

We selected 10% of the data in each of the red and NIR bands based on the AFX to compare the differences in the abilities of models with and without hotspot correction to estimate the BSA and WSA. Fig. 5 illustrates the differences in the trends of variation of the RMSEs for the BSA as the SZA increases and WSA between models with and without hotspot-corrected kernels in the red and NIR bands. Although, in the red band, the RMSEs for BSA estimation

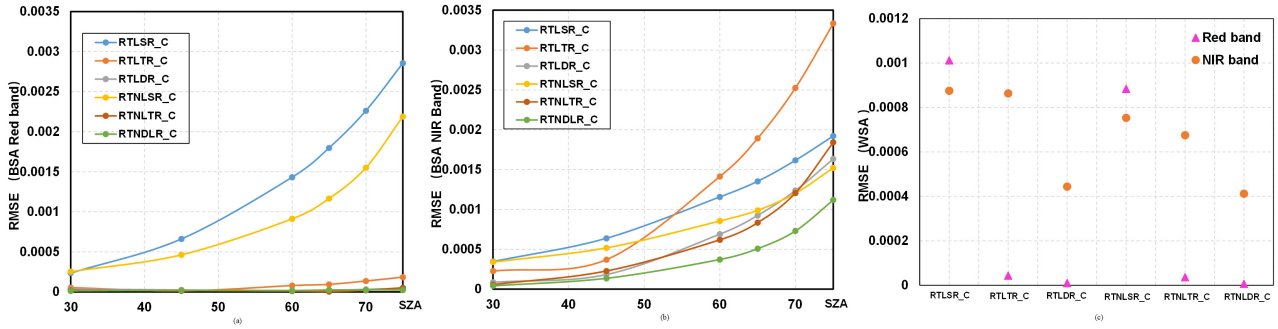

Fig. 5. Lines represent the differences between the RMSEs for BSA estimates obtained using models with and without hotspot correction at SZAs ranging from 30° to 75° in the red and NIR bands. The solid triangles and solid circles represent the RMSE differences for WSA estimates obtained using models with and without hotspot correction in the red band and the NIR band. (a) and (b) Differences between RMSEs for BSA estimates obtained using models with and without hotspot correction at SZAs ranging from 30° to 75° in the red and NIR bands, respectively. (c) Differences between RMSEs for WSA estimates obtained using models with and without hotspot correction in the red band (solid triangles) and the NIR band (solid circles).

with RTLSR_C and RTNLSR_C show the most increasing trends with increasing SZA, a significant difference between the models with and without hotspot correction appears only in the case of RTLSR_C at a large SZA, i.e., SZA = 75°, according to the *t*-test results. RTLSR and RTLSR_C also have the largest RMSEs for WSA estimation, while the RMSEs of the other four models are very small, indicating a nonsignificant difference between the versions of these models with and without hotspot correction. The trends of variation for these models in the NIR band are similar to those in the red band although the models with the LTR and LDR kernels tend to show a dramatic increase in the RMSEs for BSA estimation at SZA > 45° relative to those in the red band. However, in the NIR band, there are no significant differences in the BSA estimates between models with and without hotspot correction for all six models according to the *t*-test results. In general, the trends of variation of the RMSEs for WSA estimation in the NIR band are the same as those in the red band although the difference in RMSE between different models decreases. The overall trends of the RMSEs for albedo estimation between models with and without hotspot correction indicate an increasing difference with increasing SZA. This finding suggests that it should be possible to use hotspot-corrected kernels to compensate for the underestimation of the albedo in the original models without hotspot correction, particularly at large SZAs [41].

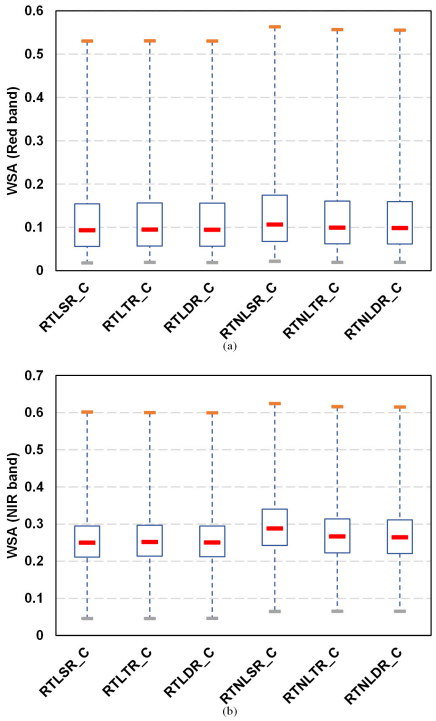

Fig. 6. Statistics of the WSA estimates in the red and NIR bands. The orange and gray sticks represent the maximum and minimum values. The red sticks represent the median values. (a) and (b) Statistics of the WSA estimates in the red and NIR bands, respectively.

D. Differences in Albedo Estimates Between the RTLSR_C Model and the Other Models

To compare the albedos calculated using the RTLSR_C model and the other hotspot-corrected models, we present only the statistics for the WSA estimates in the red and NIR bands. As shown in Fig. 6, because the WSA is a simple constant and does not vary with the SZA, the average WSA in the NIR band is nearly twice that in the red band, apparently because of the large reflectance of various vegetation types in the NIR band. The models based on the same volumetric scattering kernel in the kernel-driven framework yield similar WSAs; however, the models with the RTNC kernel tend to overestimate the WSAs relative to models with the RTC kernel. This is because the RTNC kernel tends to result in a more prominently bowl-shaped BRDF curve than the RTC kernel does (see Fig. 2). According to the *t*-test results for comparisons between two models with either the same volumetric scattering kernel or the same GO kernel, we find that the average WSA estimates produced by models with the RTC kernel are not significantly different from those produced by models with the RTC kernel in either band. Again, the differences between the RTNLSR_C model and the other models in terms of WSA estimation can be reasonably explained by the more prominently bowl-shaped pattern of the RTNC kernel at large VZAs. In general, the comparisons between the RTLSR_C model and other models with either the same volumetric scattering kernel or the same GO kernel

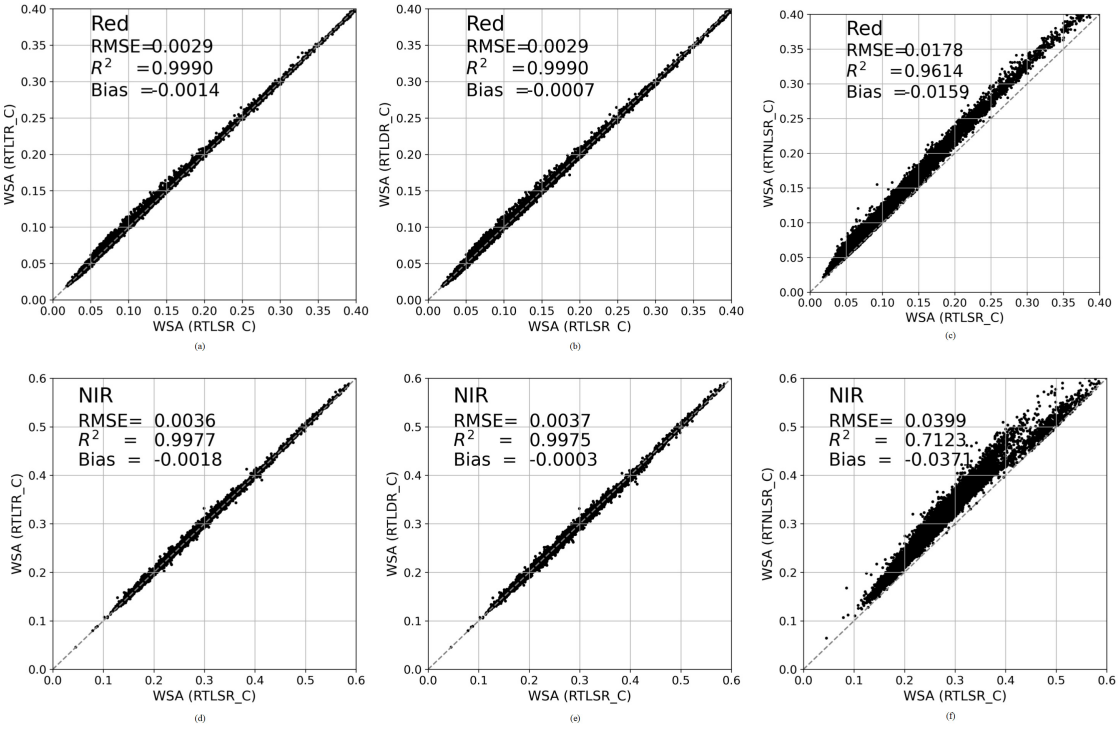

Fig. 7. Comparisons of WSA estimates between the RTLSR_C model and other models using either different volumetric scattering kernels or different GO kernels in (a)–(c) red and (d)–(f) NIR bands.

show rather high levels of correlation, with $R^2 > 0.9$, although the WSA estimates obtained using RTNLSR_C are somewhat higher than those obtained using the RTLSR_C model [see Fig. 7(c) and (f)].

In theory, the BSA tends to increase as the SZA increases [41]. Fig. 8 shows how the BSA estimates of these six models vary with the SZA and the differences between them based on only the POLDER observations selected with respect to a given AFX threshold from the entire POLDER archive; 10% of the POLDER data in each of the red and NIR bands were selected based on the AFX. The BSAs in the NIR band are obviously greater than those in the red band because of the higher reflectance of vegetation in the NIR band, and the differences between the models are more prominent in the NIR band. The BSAs increase as the direction of illumination from the sun becomes farther from the zenith direction in both the red and NIR bands.

Fig. 8(a) and (d) shows the BSA estimates from the six models for SZAs ranging from 0° to 75°. The BSAs estimated by the different models are very similar to each other when the SZA is small; although the BSAs seem to be somewhat underestimated by the RTLSR_C model (red triangles and lines), in general, there is no significant difference in the BSA estimates among the different models at SZA < 60°. At SZA > 60°, the differences in the BSA estimates, particularly between RTNLSR_C (green lines) and the other models, present a significant increasing trend. Fig. 8 shows that the other models tend to yield higher BSA estimates than the RTLSR_C model does in an SZA range of 0°–60° in both bands. At SZA > 60°, the models in which the RTNC kernel is used as the volumetric scattering kernel usually produce larger BSA estimates. The t-test results show that the BSA estimates of all the other models are significantly different from those of the RTLSR_C model at SZA > 60° in the NIR band. By contrast, in the red band, although the BSA estimates generated by RTNLSR_C show significant differences at SZA > 60°, the other models do not show a significant difference in BSA estimation relative to the RTLSR_C model until the range of SZA > 75°.

Fig. 8(b) and (e) shows the differences in the BSA estimates between each of the other five models and RTLSR_C in the red and NIR bands. The differences that exhibit similar trends of variation are presented in similar colors. It is clear that the BSA estimates generated by models with either the LTRC or LDRC kernel as the GO kernel and the same volumetric scattering kernel exhibit similar trends of variation with an increasing SZA. In general, the models with the same GO kernel but different volumetric scattering kernels (RTC or RTNC) tend to present markedly different trends. The differences between the models with the RTC kernel and the RTLSR_C model (blue lines) become even smaller as the SZA increases, while the differences between the models with the RTNC kernel and the RTLSR_C model (green and yellow lines) become larger at SZA > 60°. The differences in the BSA estimates between RTLTR_C/RTLDR_C and RTLSR_C are approximately equivalent to the differences between the LTRC/LDRC kernels and the LSRC kernel.

From the perspective of the analysis of the kernel shape as a function of the SZA (see Fig. 2), we can see that, compared with the dome-shaped LSRC kernel, the LTRC/LDRC kernels tend to exhibit a somewhat flatter shape at large VZAs; however, the LSRC kernel tends to show a more prominent increase along the backward scattering direction than the other two kernels as the SZA increases, especially at SZA > 60°.

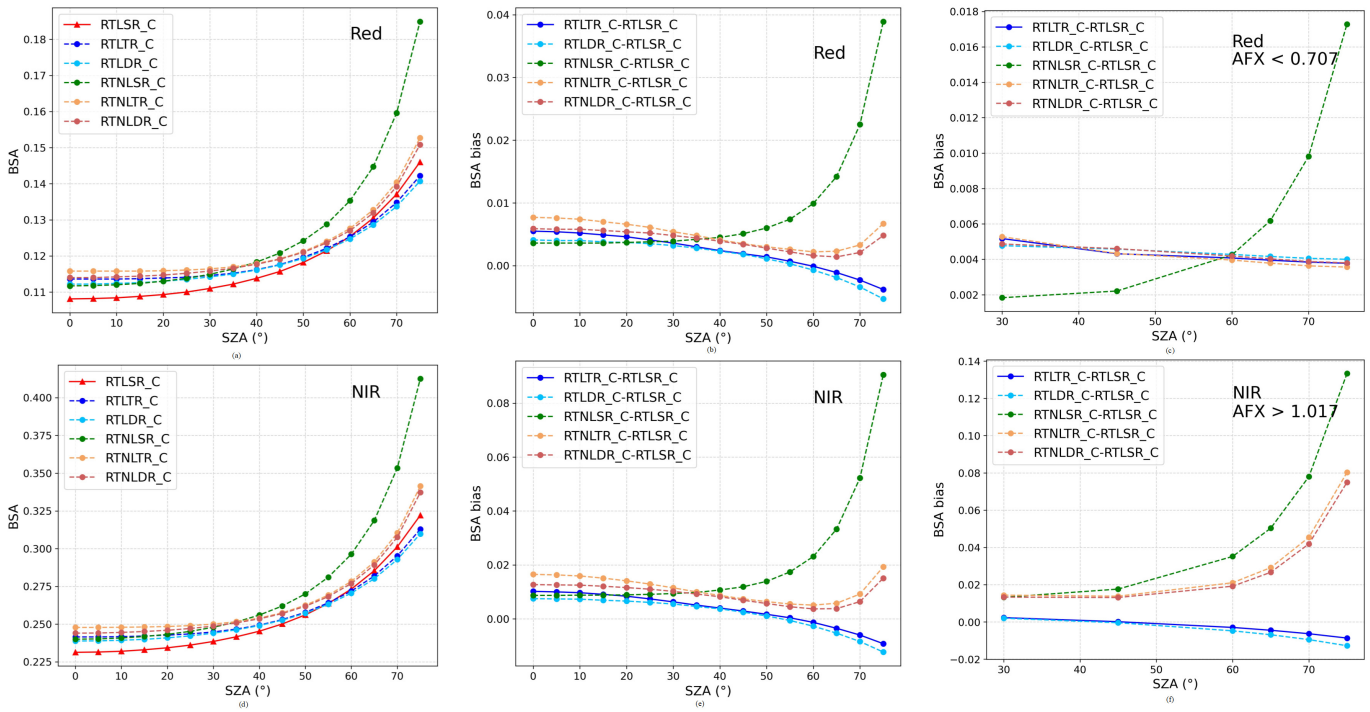

Fig. 8. (a) and (d) BSA estimates obtained using the six hotspot-corrected Ross–Li models at SZAs varying from 5° to 75°. (b) and (e) Differences in the BSA estimates between the RTLSR_C model and the other investigated models. Similar trends of variation are presented in similar colors. (c) and (f) Results analogous to those in the middle figures except that only a subset of the POLDER data, selected based on the AFX, is used, where the selected data present more prominent dome/bowl-shaped BRDF curves. In these plots, only the SZA range from 30° to 75° is considered because of the nonsignificant differences at SZA $< 30°$.

The differences between the RTNLTR_C/RTNLDR_C and RTLSR_C models (yellow lines) are similar in magnitude to the differences between the RTNC and RTC kernels and between the LTRC/LDRC kernels and the LSRC kernel. This can be reasonably explained by a similar analysis of the corresponding BRDF shapes of these kernels, which, in turn, has an influence on the modeled shape. For example, the differences in the BSA estimates between the RTNLSR_C and RTLSR_C models, which are represented by the green lines, show a dramatically increasing trend at SZA $> 60°$ relative to the differences with respect to RTNLTR_C and RTNLDR_C [see Fig. 8(b) and (e)]. These results are caused by using RTN as the volumetric scattering kernel while keeping LSR as the GO kernel in the kernel-driven model framework. These findings can be further validated by using the AFX to select data with more prominent BRDF shapes, as shown in Fig. 8(c) and (f). When these AFX-selected data are utilized, the trends caused by the BRDF shapes of the relative kernels are also more prominent. For example, in the NIR band, the differences between RTNLTR_C/RTNLDR_C and RTLSR_C [yellow lines in Fig. 8(c) and (f)] are similar, and the differences between RTLTR_C/RTLDR_C and RTLSR_C [blue lines in Fig. 8(c) and (f)] are also similar. However, these two groups of BSA estimate differences present opposite trends as a result of the different trends of variation in the kernel shapes of the RTC and RTNC models as the SZA increases [see Fig. 2(a)]. In summary, through a comparison of the BSA estimates generated by these models using POLDER data, together with an analysis of the variability in the kernel shapes as a function of the SZA, we can see that appropriate combinations of various Ross–Li kernels can provide an improved understanding of the estimated albedos (e.g., the BSA here) and, in particular, can provide a way to address the underestimation of the albedo at large SZAs of $> 70°$.

E. Comparison of POLDER Albedo Estimates With Concurrent MODIS Data

Comparison of BSA estimated by the six improved models with POLDER data and the MODIS BSA product at local solar noon is shown in Fig. 9. The range of MODIS local solar noon varies from 1.8° to 61.4°. The biases in the red and NIR bands are positive for all models, which means that the hotspot-improved models have larger BSA estimations than the MODIS algorithm when the SZAs are smaller than 60°. The models that are composed of the RossThinChen kernel have a higher bias than models that are composed of the RossThickChen kernel. This result confirms the ability of the improved models to solve the slight underestimation of MODIS albedo that was found in the previous study [41].

To further examine the potential differences in terms of BSA estimation in the large-SZA range of 60°–75° for each of the other investigated models relative to the RTLSR model, Fig. 10 shows the scatterplots that compare the BSAs simulated with the RTLSR model using the operational MODIS BRDF parameter product against the BSAs estimated with all the other Ross–Li models using the concurrent POLDER data in the red and NIR bands. From Fig. 10, we can see

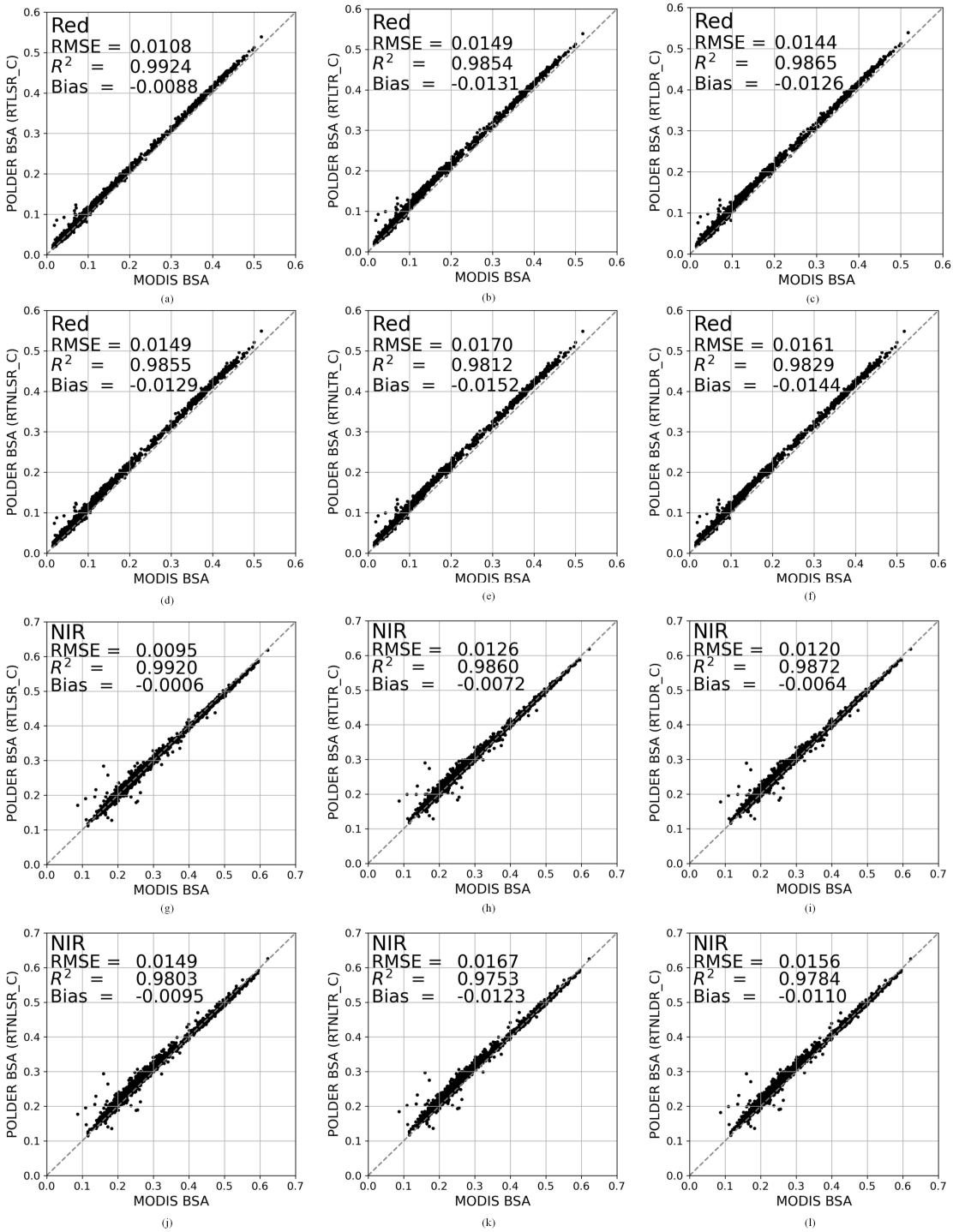

Fig. 9. Comparison of BSA estimates obtained from the coarse-resolution POLDER data using the six models (on the vertical axis) and the corresponding 13×13 finer resolution MODIS data calculated with RTLSR_C (on the horizontal axis) at local solar noon. (a) and (g) Comparisons between BSA estimates obtained from POLDER data using RTLSR_C and the corresponding MODIS BSA in the red and NIR bands, respectively. (b) and (h) Comparisons between BSA estimates obtained from POLDER data using RTLTR_C and the corresponding MODIS BSA in the red and NIR bands, respectively. (c) and (i) Comparisons between BSA estimates obtained from POLDER data using RTLDR_C and the corresponding MODIS BSA in the red and NIR bands, respectively. (d) and (j) Comparisons between BSA estimates obtained from POLDER data using RTNLSR_C and the corresponding MODIS BSA in the red and NIR bands, respectively. (e) and (k) Comparisons between BSA estimates obtained from POLDER data using RTNLTR_C and the corresponding MODIS BSA in the red and NIR bands, respectively. (f) and (l) Comparisons between BSA estimates obtained from POLDER data using RTNLDR_C and the corresponding MODIS BSA in the red and NIR bands, respectively. All these BSA estimates are at local solar noon.

that the BSA estimates obtained by applying the RTLSR model to the MODIS data and those obtained by applying the other investigated models to the POLDER data are generally consistent (with a large R^2); however, the biases depend on the selected model. The models with the RTC kernel as K_{vol} have a BSA estimation ability similar to that of the RTLSR model in both bands (the first and third rows in Fig. 10) although some differences also exist between the two bands. In the red band,

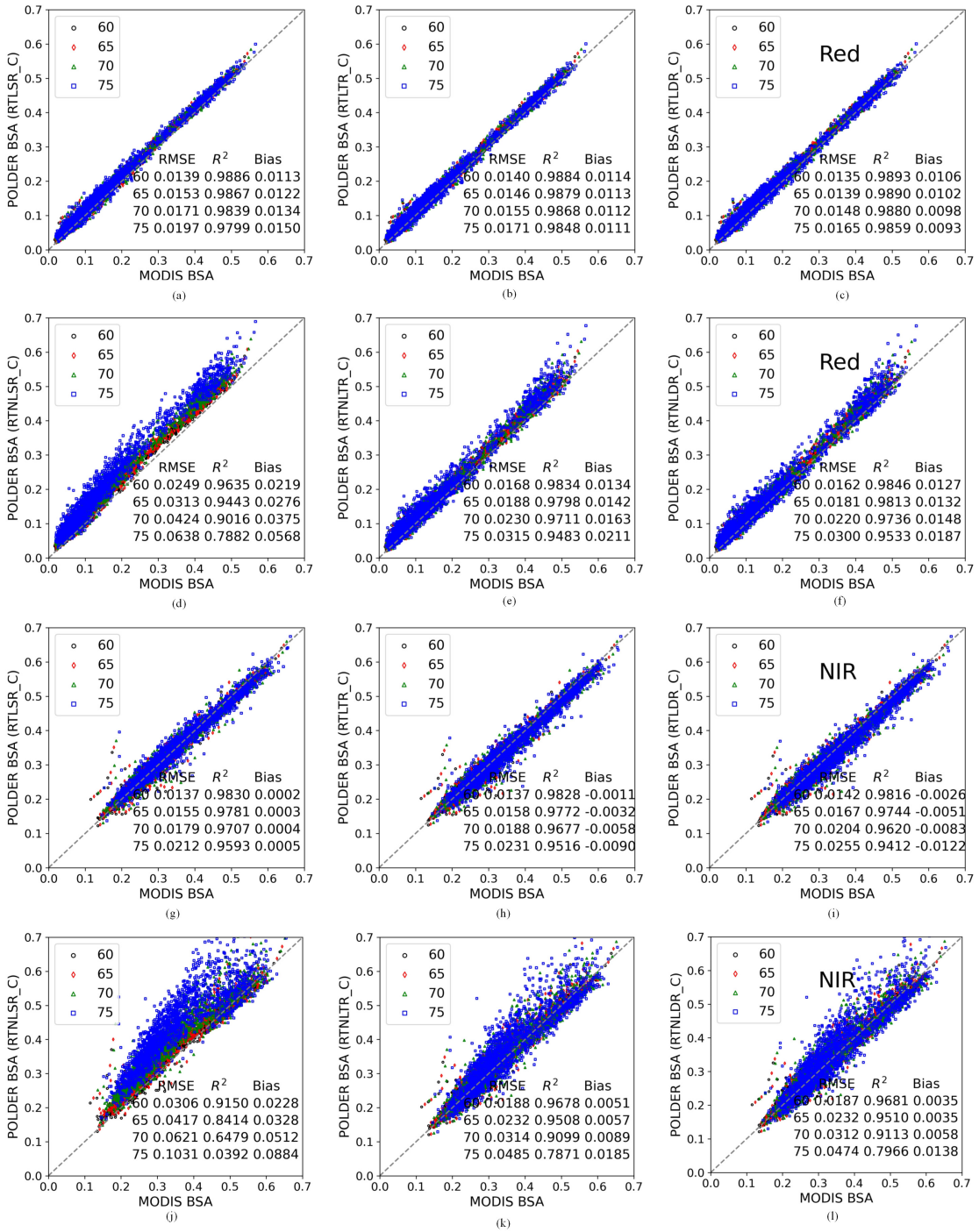

Fig. 10. Comparison of BSA estimates obtained from the coarse-resolution POLDER data using the six models (on the vertical axis) and the corresponding 13×13 finer resolution MODIS data calculated with RTLSR (on the horizontal axis) in the large-SZA range of 60°–75°. The black points represent BSAs at SZA = 60°, the red points represent BSAs at SZA = 65°, the cyan points represent BSAs at SZA = 70°, and the blue points represent BSAs at SZA = 75°. (a) and (g) Comparisons between BSA estimates obtained from POLDER data using RTLSR_C and the corresponding MODIS BSA in the red and NIR bands, respectively. (b) and (h) Comparisons between BSA estimates obtained from POLDER data using RTLTR_C and the corresponding MODIS BSA in the red and NIR bands, respectively. (c) and (i) Comparisons between BSA estimates obtained from POLDER data using RTLDR_C and the corresponding MODIS BSA in the red and NIR bands, respectively. (d) and (j) Comparisons between BSA estimates obtained from POLDER data using RTNLSR_C and the corresponding MODIS BSA in the red and NIR bands, respectively. (e) and (k) Comparisons between BSA estimates obtained from POLDER data using RTNLTR_C and the corresponding MODIS BSA in the red and NIR bands, respectively. (f) and (l) Comparisons between BSA estimates obtained from POLDER data using RTNLDR_C and the corresponding MODIS BSA in the red and NIR bands, respectively.

the BSA estimates obtained by applying models with the RTC kernel to the POLDER data are somewhat higher than those obtained by applying the RTLSR_C model to the MODIS data. By contrast, the models with the RTNC kernel applied to the POLDER data show significant overestimation of the BSA. Compared with the results obtained from the RTLSR model using the MODIS data, in the NIR band, this overestimation increases as the SZA increases from 60° to 75°; in particular,

TABLE III
COMPARISON OF THE SIMULATED AND OBSERVED ALBEDO

	Site	1	2	3	4	5	6	7	8
	SZA (°)	30.025	30.051	45.094	45.057	60.098	60.045	74.547	74.011
Albedo	RTNLSR_C	0.11510	0.16898	0.16497	0.20032	0.18702	0.20148	0.12704	0.21498
	RTLSR	0.11813	0.16331	0.14445	0.17158	0.18013	0.20969	0.10359	0.17197
	observations	0.11522	0.12382	0.19768	0.15733	0.21860	0.22071	0.11514	0.24847
	Bias (RTNLSR_C)	0.00078	0.04516	-0.03271	0.04299	-0.03158	-0.01923	*0.01191*	*-0.03350*
	Bias (RTLSR)	0.00292	0.03949	-0.05324	0.01425	-0.03847	-0.01102	-0.01155	-0.07650

the RTNLSR_C estimates present markedly larger differences relative to the RTLSR estimates with the bias increasing from 0.02 to 0.08. According to the direct comparison between the MODIS albedo and ground measurements, the biases are approximately negative 0.02–0.08 at large SZAs [41]. This finding provides further evidence that a model with a suitable combination of the Ross–Li kernels, e.g., the RTNLSR_C model here, can provide a way to improve the somewhat underestimated albedos at large SZAs (e.g., SZA $>$ 75°) that have been noted by the MODIS albedo product team [41].

F. Validation of RTNLSR_C Model Using Albedo Observations

The comparison of albedo simulated by RTNLSR_C and MODIS albedo products with albedo observations is shown in Table III. The comparison results show that, when SZA $\leq$ 60°, the albedos simulated by RTNLSR_C or RTLSR model are similar. Compared with the site observations, the simulated albedos have the same negative or positive bias trend as observations. When SZA $=$ 75°, albedo estimation by the RTNLSR_C model is higher than MODIS products and is closer to albedo measurements derived from the network sites, which further confirms the conclusion that the RTNLSR_C model has the potential to solve the underestimation of albedo at large SZAs. This effort proves that the RTNLSR_C model performs better with respect to estimating albedo at large SZAs.

V. DISCUSSION

In this study, we have comprehensively assessed the improved Ross–Li series of the kernel-driven models using the entire POLDER BRDF archive. In particular, we have analyzed the capabilities of these models in regard to the estimation of the intrinsic albedo of the land surface, with an emphasis on the comparison and analysis of the variability in the BSA estimates as a function of the SZA in the large-SZA range of 60°–75°. Our intent was to revisit the strategy proposed early by the MODIS BRDF/albedo team to identify which improved Ross–Li series models show the best potential to correct the underestimation of the retrieval albedo (particularly the BSA) at large SZAs. The main finding of this study is that, among the improved Ross–Li models under investigation, the RTLSR_C model (i.e., the operational MODIS BRDF algorithm with hotspot-corrected kernel functions) shows the best performance in fitting the entire POLDER BRDF archive and, thus, in estimating the intrinsic land surface albedos. Furthermore, our results also show that the models that include the RTNC kernel are most likely to successfully correct the underestimation of the intrinsic albedo of the operational RTLSR algorithm in the large-SZA range.

However, some potential problems must be further discussed here. First, the BRDF sampling capabilities of the MODIS sensors are limited, particularly for the acquisition of observations near the hotspot direction and in the VZA range $>$ 60°. Considering this potential problem, we adopted all data from two POLDER data sets to obtain multiangular observations with good BRDF sampling in these two regimes in order to comprehensively assess six recently hotspot-improved Ross–Li models. The data sets selected from the POLDER database for this purpose have wide angular ranges, e.g., the SZAs are as large as 75°, and the VZAs reach 70°. Observations at such angles can more effectively constrain the models under investigation that cannot be achieved using the MODIS data [71]; as a result, it is expected that the intrinsic albedo (particularly the BSA) of the land surface can be more accurately estimated. In addition, a larger quantity of observations near the hotspot direction can similarly provide better constraints to optimize the hotspot parameters, which, in theory, should help to further improve the accuracy of intrinsic albedo estimation. Therefore, the use of the POLDER observations to assess the recently hotspot-improved Ross–Li models can be reasonably expected to yield additional significant findings compared with many similar studies previously reported in this domain (e.g., [38], [39], and [41]). Nevertheless, we note that there is a potential limitation related to the common problems with multiangular observations. For example, because of the wide FOV of POLDER (up to 70°), there is an enormous difference between nadir observations and nonnadir observations [3]. Such inherent characteristics of multiangular observations will inevitably lead to some level of error.

In addition, some uncertainty arises in assessing the variability in albedo estimates using the 6×7 km POLDER pixels due to their coarse spatial resolution, which is likely to result in mixed pixels that include various land cover types to some degree; especially, at large VZA, the larger footprint makes it more difficult to guarantee surface homogeneity. To address this uncertainty, in this study, MODIS BRDF products with a 500-m spatial resolution were initially utilized as constraints to select high-quality POLDER pixels and were also used as a benchmark to assess the albedo estimates from the concurrent POLDER pixels. In our previous study, we confirmed that the arrays of 13×13 MODIS pixels can be very well matched to single POLDER pixels [50] by using various prior information (e.g., BRDF quality flag products, MODIS land cover products, and MODIS VCF products) [60]. Notably, this study presents only an indirect comparison between the results

obtained using the MODIS BRDF products and those obtained using the POLDER observations as evidence. It is still difficult to acquire representative *in situ* albedo measurements within a footprint as large as 6×7 km (or even larger at large VZAs) for further validation. Notably, since acquiring the same multiangular reflectance data as the operational MODIS BRDF/albedo product does is an extreme challenge, the validation of the RTNLSR_C model by directly using original multiangular MODIS reflectance is not performed in this study. (However, we proposed the method to indirectly apply RTNLSR_C model in conjunction with MODIS BRDF data to estimate albedo and compare it with site observations and MODIS albedo products, which further confirms our results based on the POLDER data.)

Although BRDF and surface types describe different aspects of the surface, the relationship between these improved kernels and surface types still needs further construction since the kernels mutually complement each other in depicting the characteristic of BRDF.

Despite the potential uncertainties, the POLDER database provides highly valuable data with good BRDF sampling characteristics, especially in the hotspot direction and for large-angle view geometries, on the global scale. Moreover, the potential uncertainties associated with these POLDER data should have almost the same influence on each of the models explored in this study; therefore, these uncertainties should be largely offset in comparisons between models. Hence, it can be concluded that the results presented here are probably credible and thus helpful for guiding potential users in applying these models for various purposes in the future.

VI. Conclusion

In this study, in order to address the underestimation problem of MODIS albedo at a large SZA, which was reported early in some studies, we used POLDER data to assess the performance of six hotspot-corrected Ross–Li models. We relied on the calculated RMSE and RMSE_*r* values to evaluate the reflectance fitting ability. To explore the problem that the default MODIS intrinsic albedo products (particularly the BSA) are likely underestimated by the operational RTLSR model in the large-SZA range of $>70°$, we focused on comparing the BSA and WSA estimates obtained by applying these models to the entire POLDER archive with the corresponding aggregated MODIS products calculated at a similar spatial resolution. The main findings are as follows.

1) The fitting accuracy of the RTLSR_C model (i.e., the operational RTLSR model with hotspot-corrected kernel functions) is the best among all of the investigated models (including the RTLSR model), thus confirming the results of several early studies that mainly relied on various collected field measurements [3], [38], [39].
2) The hotspot correction on Ross–Li models has an influence on albedo estimation, especially at large SZAs.
3) Furthermore, in the large-SZA range of 60°–75°, models that include the RTNC kernel show an appropriate overestimation (with biases varying from 0.02 to 0.08) of the BSAs relative to the operational MODIS BRDF/albedo algorithm (i.e., RTLSR), according to a comparison of the intrinsic albedo estimates obtained using the coarse POLDER data with the aggregated corresponding MODIS BRDF products. Therefore, such models may provide a way to compensate for the albedo underestimation of the operational model at large SZAs that have been reported in previous studies (e.g., [41]).

Notably, although we have revisited the performance of these improved Ross–Li models and presented a promising way to improve the intrinsic albedo estimation at large SZAs using the POLDER data, it will likely still be a challenge to use these models in an operational fashion because the overwhelming majority of current multiangular sensors rarely capture observations as wide a range of viewing angles as those available in the POLDER data explored here. Therefore, the development of a strategy for effectively using such prior knowledge in such situations will be extremely important in the near future.

Acknowledgment

The POLDER-3/PARASOL BRDF databases were elaborated by the Laboratoire des Sciences du Climat et de l'Environment (LSCE) and were provided by the POSTEL Service Center. The authors would like to thank the research team of the MODIS BRDF/Albedo products for the long-term cooperation and assistance in the kernel-driven model improvement and development.

References

[1] R. E. Dickinson, "Land processes in climate models," *Remote Sens. Environ.*, vol. 51, no. 1, pp. 27–38, Jan. 1995, doi: 10.1016/0034-4257(94)00062-R.

[2] G. Schaepman-Strub, M. E. Schaepman, T. H. Painter, S. Dangel, and J. V. Martonchik, "Reflectance quantities in optical remote sensing—Definitions and case studies," *Remote Sens. Environ.*, vol. 103, no. 1, pp. 27–42, Jul. 2006, doi: 10.1016/j.rse.2006.03.002.

[3] W. Lucht, C. B. Schaaf, and A. H. Strahler, "An algorithm for the retrieval of albedo from space using semiempirical BRDF models," *IEEE Trans. Geosci. Remote Sens.*, vol. 38, no. 2, pp. 977–998, Mar. 2000, doi: 10.1109/36.841980.

[4] K. T. Kriebel, "Albedo of vegetated surfaces: Its variability with differing irradiances," *Remote Sens. Environ.*, vol. 8, no. 4, pp. 283–290, Dec. 1979, doi: 10.1016/0034-4257(79)90028-2.

[5] C. L. Walthall, J. M. Norman, J. M. Welles, G. Campbell, and B. L. Blad, "Simple equation to approximate the bidirectional reflectance from vegetative canopies and bare soil surfaces," *Appl. Opt.*, vol. 24, no. 3, pp. 383–387, Feb. 1985, doi: 10.1364/AO.24.000383.

[6] K. J. Ranson, J. R. Irons, and C. S. T. Daughtry, "Surface albedo from bidirectional reflectance," *Remote Sens. Environ.*, vol. 35, nos. 2–3, pp. 201–211, Feb./Mar. 1991, doi: 10.1016/0034-4257(91)90012-U.

[7] F. Cabot and G. Dedieu, "Surface albedo from space: Coupling bidirectional models and remotely sensed measurements," *J. Geophys. Res., Atmos.*, vol. 102, no. D16, pp. 19645–19663, Aug. 1997, doi: 10.1029/97JD00085.

[8] *The Global Observing System for Climate: Implementation Needs*, Global Climate Observing System, WMO, Geneva, Switzerland, 2016.

[9] P. Sellers *et al.*, "Remote sensing of the land surface for studies of global change: Models-algorithms-experiments," *Remote Sens. Environ.*, vol. 51, no. 1, pp. 3–26, Jan. 1995, doi: 10.1016/0034-4257(94)00061-Q.

[10] P. J. Lawrence and T. N. Chase, "Representing a new MODIS consistent land surface in the community land model (CLM 3.0)," *J. Geophys. Res.*, vol. 112, no. G1, Mar. 2007, Art. no. G01023, doi: 10.1029/2006JG000168.

[11] O. Samain, B. Geiger, and J.-L. Roujean, "Spectral normalization and fusion of optical sensors for the retrieval of BRDF and albedo: Application to VEGETATION, MODIS, and MERIS data sets," *IEEE Trans. Geosci. Remote Sens.*, vol. 44, no. 11, pp. 3166–3179, Nov. 2006, doi: 10.1109/TGRS.2006.879545.

[12] X. Li, F. Gao, J. Wang, and A. Strahler, "A Priori knowledge accumulation and its application to linear BRDF model inversion," *J. Geophys. Res., Atmos.*, vol. 106, no. D11, pp. 11925–11935, Jun. 2001, doi: 10.1029/2000jd900639.

[13] F. Gao, "MODIS bidirectional reflectance distribution function and albedo climate modeling grid products and the variability of albedo for major global vegetation types," *J. Geophys. Res.*, vol. 110, no. D1, 2005, Art. no. D01104, doi: 10.1029/2004JD005190.

[14] Y. Shuai, J. G. Masek, F. Gao, and C. B. Schaaf, "An algorithm for the retrieval of 30-m snow-free albedo from Landsat surface reflectance and MODIS BRDF," *Remote Sens. Environ.*, vol. 115, no. 9, pp. 2204–2216, Sep. 2011, doi: 10.1016/j.rse.2011.04.019.

[15] Y. Shuai, J. G. Masek, F. Gao, C. B. Schaaf, and T. He, "An approach for the long-term 30-m land surface snow-free albedo retrieval from historic Landsat surface reflectance and MODIS-based a priori anisotropy knowledge," *Remote Sens. Environ.*, vol. 152, pp. 467–479, Sep. 2014, doi: 10.1016/j.rse.2014.07.009.

[16] S. Peng *et al.*, "Multi-staged NDVI dependent snow-free land-surface shortwave albedo narrowband-to-broadband (NTB) coefficients and their sensitivity analysis," *Remote Sens.*, vol. 9, no. 1, p. 93, Jan. 2017, doi: 10.3390/rs9010093.

[17] D. Blok, G. Schaepman-Strub, H. Bartholomeus, M. M. P. D. Heijmans, T. C. Maximov, and F. Berendse, "The response of arctic vegetation to the summer climate: Relation between shrub cover, NDVI, surface albedo and temperature," *Environ. Res. Lett.*, vol. 6, no. 3, Sep. 2011, Art. no. 035502, doi: 10.1088/1748-9326/6/3/035502.

[18] Z. Jiao, H. Zhang, Y. Dong, Q. Liu, Q. Xiao, and X. Li, "An algorithm for retrieval of surface albedo from small view-angle airborne observations through the use of BRDF archetypes as prior knowledge," *IEEE J. Sel. Topics Appl. Earth Observ. Remote Sens.*, vol. 8, no. 7, pp. 3279–3293, Jul. 2015, doi: 10.1109/jstars.2015.2414925.

[19] H. Zhang, Z. Jiao, Y. Dong, and X. Li, "Evaluation of BRDF archetypes for representing surface reflectance anisotropy using MODIS BRDF data," *Remote Sens.*, vol. 7, no. 6, pp. 7826–7845, Jun. 2015, doi: 10.3390/rs70607826.

[20] H. Zhang *et al.*, "Analysis of extracting prior BRDF from MODIS BRDF data," *Remote Sens.*, vol. 8, no. 12, p. 1004, Dec. 2016, doi: 10.3390/rs8121004.

[21] Z. Jiao *et al.*, "A method for improving hotspot directional signatures in BRDF models used for MODIS," *Remote Sens. Environ.*, vol. 186, pp. 135–151, Dec. 2016, doi: 10.1016/j.rse.2016.08.007.

[22] S. Liang, "A direct algorithm for estimating land surface broadband albedos from MODIS imagery," *IEEE Trans. Geosci. Remote Sens.*, vol. 41, no. 1, pp. 136–145, Jan. 2003, doi: 10.1109/TGRS.2002.807751.

[23] S. Liang, A. Strahler, and C. Walthall, "Retrieval of land surface albedo from satellite observations: A simulation study," in *Proc. Sens. Manag. Environ., IEEE Int. Geosci. Remote Sens. Symp. (IGARSS)*, Seattle, WA, USA, Jul. 1998, pp. 1286–1288, doi: 10.1109/IGARSS.1998.691379.

[24] T. He, S. Liang, and D. Wang, "Direct estimation of land surface albedo from simultaneous MISR data," *IEEE Trans. Geosci. Remote Sens.*, vol. 55, no. 5, pp. 2605–2617, May 2017, doi: 10.1109/TGRS.2017.2648847.

[25] D. Wang, S. Liang, T. He, and Y. Yu, "Direct estimation of land surface albedo from VIIRS data: Algorithm improvement and preliminary validation," *J. Geophys. Res., Atmos.*, vol. 118, no. 22, pp. 12577–12586, Nov. 2013, doi: 10.1002/2013JD020417.

[26] X. Zhang *et al.*, "Development of the direct-estimation albedo algorithm for snow-free Landsat TM albedo retrievals using field flux measurements," *IEEE Trans. Geosci. Remote Sens.*, vol. 58, no. 3, pp. 1550–1567, Mar. 2020, doi: 10.1109/TGRS.2019.2946598.

[27] H. Rahman, B. Pinty, and M. M. Verstraete, "Coupled surface-atmosphere reflectance (CSAR) model. 2: Semiempirical surface model usable with NOAA Advanced Very High Resolution Radiometer data," *J. Geophys. Res., Atmos.*, vol. 98, no. D11, pp. 20791–20801, Nov. 1993, doi: 10.1029/93JD02072.

[28] J. L. Roujean, M. Leroy, and P. Y. Deschamps, "A bidirectional reflectance model of the earths surface for the correction of remote-sensing data," *J. Geophys. Res., Atmos.*, vol. 97, no. D18, pp. 20455–20468, Dec. 1992, doi: 10.1029/92JD01411.

[29] W. Wanner, X. Li, and A. H. Strahler, "On the derivation of kernels for kernel-driven models of bidirectional reflectance," *J. Geophys. Res., Atmos.*, vol. 100, no. D10, pp. 21077–21089, Oct. 1995, doi: 10.1029/95JD02371.

[30] X. Li, F. Gao, L. Chen, and A. H. Strahler, "Derivation and validation of a new kernel for kernel-driven BRDF models," *Proc. SPIE*, vol. 3868, pp. 368–380, Jan. 1999.

[31] J. M. Chen, C. H. Menges, and S. G. Leblanc, "Global mapping of foliage clumping index using multi-angular satellite data," *Remote Sens. Environ.*, vol. 97, no. 4, pp. 447–457, Sep. 2005, doi: 10.1016/j.rse.2005.05.003.

[32] Z. Jiao *et al.*, "An algorithm for the retrieval of the clumping index (CI) from the MODIS BRDF product using an adjusted version of the kernel-driven BRDF model," *Remote Sens. Environ.*, vol. 209, pp. 594–611, May 2018, doi: 10.1016/j.rse.2018.02.041.

[33] L. He, J. M. Chen, J. Pisek, C. B. Schaaf, and A. H. Strahler, "Global clumping index map derived from the MODIS BRDF product," *Remote Sens. Environ.*, vol. 119, pp. 118–130, Apr. 2012, doi: 10.1016/j.rse.2011.12.008.

[34] G. Zhu, W. Ju, J. M. Chen, P. Gong, B. Xing, and J. Zhu, "Foliage clumping index over China's landmass retrieved from the MODIS BRDF parameters product," *IEEE Trans. Geosci. Remote Sens.*, vol. 50, no. 6, pp. 2122–2137, Jun. 2012, doi: 10.1109/TGRS.2011.2172213.

[35] J. M. Chen and J. Cihlar, "A hotspot function in a simple bidirectional reflectance model for satellite applications," *J. Geophys. Res., Atmos.*, vol. 102, no. D22, pp. 25907–25913, Nov. 1997, doi: 10.1029/97JD02010.

[36] F. Maignan, F.-M. Bréon, and R. Lacaze, "Bidirectional reflectance of Earth targets: Evaluation of analytical models using a large set of spaceborne measurements with emphasis on the hot spot," *Remote Sens. Environ.*, vol. 90, no. 2, pp. 210–220, Mar. 2004, doi: 10.1016/j.rse.2003.12.006.

[37] Y. Dong *et al.*, "A visualization tool for the kernel-driven model with improved ability in data analysis and kernel assessment," *Comput. Geosci.*, vol. 95, pp. 1–10, Oct. 2016, doi: 10.1016/j.cageo.2016.06.010.

[38] B. Hu, W. Lucht, X. Li, and A. H. Strahler, "Validation of kernel-driven semiempirical models for the surface bidirectional reflectance distribution function of land surfaces," *Remote Sens. Environ.*, vol. 62, no. 3, pp. 201–214, Dec. 1997.

[39] X. Huang, Z. Jiao, Y. Dong, H. Zhang, and X. Li, "Analysis of BRDF and albedo retrieved by kernel-driven models using field measurements," *IEEE J. Sel. Topics Appl. Earth Observ. Remote Sens.*, vol. 6, no. 1, pp. 149–161, Feb. 2013, doi: 10.1109/JSTARS.2012.2208264.

[40] Y. Jin, "Consistency of MODIS surface bidirectional reflectance distribution function and albedo retrievals: 1. Algorithm performance," *J. Geophys. Res.*, vol. 108, no. D5, p. 4158, 2003, doi: 10.1029/2002jd002803.

[41] J. Liu *et al.*, "Validation of Moderate Resolution Imaging Spectroradiometer (MODIS) albedo retrieval algorithm: Dependence of albedo on solar zenith angle," *J. Geophys. Res., Atmos.*, vol. 114, no. D1, Jan. 2009, Art. no. D01106, doi: 10.1029/2008jd009969.

[42] M. O. Román, C. K. Gatebe, C. B. Schaaf, R. Poudyal, Z. Wang, and M. D. King, "Variability in surface BRDF at different spatial scales (30 m–500 m) over a mixed agricultural landscape as retrieved from airborne and satellite spectral measurements," *Remote Sens. Environ.*, vol. 115, no. 9, pp. 2184–2203, Sep. 2011, doi: 10.1016/j.rse.2011.04.012.

[43] Z. Wang *et al.*, "Evaluation of MODIS albedo product (MCD43A) over grassland, agriculture and forest surface types during dormant and snow-covered periods," *Remote Sens. Environ.*, vol. 140, pp. 60–77, Jan. 2014, doi: 10.1016/j.rse.2013.08.025.

[44] Z. Wang, C. B. Schaaf, Q. Sun, Y. Shuai, and M. O. Román, "Capturing rapid land surface dynamics with collection V006 MODIS BRDF/NBAR/Albedo (MCD43) products," *Remote Sens. Environ.*, vol. 207, pp. 50–64, Mar. 2018, doi: 10.1016/j.rse.2018.02.001.

[45] A. Ding *et al.*, "Evaluation of the snow albedo retrieved from the snow kernel improved the ross-roujean BRDF model," *Remote Sens.*, vol. 11, no. 13, p. 1611, Jul. 2019, doi: 10.3390/rs11131611.

[46] A. Ding *et al.*, "An assessment of the performance of two snow kernels in characterizing snow scattering properties," *Int. J. Remote Sens.*, vol. 40, no. 16, pp. 6315–6335, Aug. 2019, doi: 10.1080/01431161.2019.1590878.

[47] Z. Jiao *et al.*, "Development of a snow kernel to better model the anisotropic reflectance of pure snow in a kernel-driven BRDF model framework," *Remote Sens. Environ.*, vol. 221, pp. 198–209, Feb. 2019, doi: 10.1016/j.rse.2018.11.001.

[48] V. V. Rozanov, A. V. Rozanov, A. A. Kokhanovsky, and J. P. Burrows, "Radiative transfer through terrestrial atmosphere and ocean: Software package SCIATRAN," *J. Quant. Spectrosc. Radiat. Transf.*, vol. 133, pp. 13–71, Jan. 2014, doi: 10.1016/j.jqsrt.2013.07.004.

[49] L. Mei *et al.*, "Retrieval of aerosol optical thickness in the arctic snow-covered regions using passive remote sensing: Impact of aerosol typing and surface reflection model," *IEEE Trans. Geosci. Remote Sens.*, vol. 58, no. 7, pp. 5117–5131, Jul. 2020, doi: 10.1109/TGRS.2020.2972339.

[50] Z. Jiao *et al.*, "The influence of spatial resolution on the angular variation patterns of optical reflectance as retrieved from MODIS and POLDER measurements," *Remote Sens. Environ.*, vol. 215, pp. 371–385, Sep. 2018, doi: 10.1016/j.rse.2018.06.025.
[51] S. G. Warren and W. J. Wiscombe, "A model for the spectral albedo of snow. II: Snow containing atmospheric aerosols," *J. Atmos. Sci.*, vol. 37, no. 12, pp. 2734–2745, Dec. 1980, doi: 10.1175/1520-0469(1980)037<2734:amftsa>2.0.co;2.
[52] T. H. Painter and J. Dozier, "The effect of anisotropic reflectance on imaging spectroscopy of snow properties," *Remote Sens. Environ.*, vol. 89, no. 4, pp. 409–422, Feb. 2004, doi: 10.1016/j.rse.2003.09.007.
[53] Z. Wang, "The solar zenith angle dependence of desert albedo," *Geophys. Res. Lett.*, vol. 32, no. 5, 2005, doi: 10.1029/2004GL021835.
[54] C. Schaaf *et al.*, "Retrieval of surface albedo from satellite sensors," in *Advances in Land Remote Sensing: System, Modeling, Inversion and Application*, S. Liang, Ed. New York, NY, USA: Springer-Verlag, 2008, pp. 219–243.
[55] C. B. Schaaf, Z. Wang, and A. H. Strahler, "Commentary on wang and zender—MODIS snow albedo bias at high solar zenith angles relative to theory and to *in situ* observations in greenland," *Remote Sens. Environ.*, vol. 115, no. 5, pp. 1296–1300, May 2011, doi: 10.1016/j.rse.2011.01.002.
[56] P.-Y. Deschamps *et al.*, "The POLDER mission: Instrument characteristics and scientific objectives," *IEEE Trans. Geosci. Remote Sens.*, vol. 32, no. 3, pp. 598–615, May 1994, doi: 10.1109/36.297978.
[57] F. M. Bréon and F. Maignan, "A BRDF–BPDF database for the analysis of Earth target reflectances," *Earth Syst. Sci. Data*, vol. 9, no. 1, pp. 31–45, Jan. 2017, doi: 10.5194/essd-9-31-2017.
[58] F. M. Bréon, "PARASOL level-1 product data format and user manual," CEA/LSCE, CNES, Paris, Île-de-France, Tech. Rep., 2006, p. 31.
[59] S. Wei and H. Fang, "Estimation of canopy clumping index from MISR and MODIS sensors using the normalized difference hotspot and darkspot (NDHD) method: The influence of BRDF models and solar zenith angle," *Remote Sens. Environ.*, vol. 187, pp. 476–491, Dec. 2016, doi: 10.1016/j.rse.2016.10.039.
[60] L. Cui *et al.*, "Estimating forest canopy height using MODIS BRDF data emphasizing typical-angle reflectances," *Remote Sens.*, vol. 11, no. 19, p. 2239, Sep. 2019, doi: 10.3390/rs11192239.
[61] F. E. Nicodemus, J. C. Richmond, J. J. Hsia, I. W. Ginsberg, and T. Limperis, "Geometrical considerations and nomenclature for reflectance," Inst. Basic Standards Nat. Bur. Standards, Washington, DC, USA, Nat. Bur. Standards Rep. NBS, MN-160, 1977, p. 52.
[62] C. B. Schaaf *et al.*, "First operational BRDF, albedo nadir reflectance products from MODIS," *Remote Sens. Environ.*, vol. 83, nos. 1–2, pp. 135–148, Nov. 2002, doi: 10.1016/S0034-4257(02)00091-3.
[63] W. Lucht, A. H. Hyman, A. H. Strahler, M. J. Barnsley, P. Hobson, and J. P. Muller, "A comparison of satellite-derived spectral albedos to ground-based broadband albedo measurements modeled to satellite spatial scale for a semidesert landscape," *Remote Sens. Environ.*, vol. 74, no. 1, pp. 85–98, Oct. 2000, doi: 10.1016/S0034-4257(00)00125-5.
[64] M. A. Friedl *et al.*, "MODIS collection 5 global land cover: Algorithm refinements and characterization of new datasets," *Remote Sens. Environ.*, vol. 114, no. 1, pp. 168–182, Jan. 2010, doi: 10.1016/j.rse.2009.08.016.
[65] M. C. Hansen, R. S. DeFries, J. R. G. Townshend, R. Sohlberg, C. Dimiceli, and M. Carroll, "Towards an operational MODIS continuous field of percent tree cover algorithm: Examples using AVHRR and MODIS data," *Remote Sens. Environ.*, vol. 83, nos. 1–2, pp. 303–319, Nov. 2002, doi: 10.1016/S0034-4257(02)00079-2.
[66] X. Li, F. Gao, J. Wang, A. H. Strahler, W. Lucht, and C. Schaaf, "Estimation of the parameter error propagation in inversion based BRDF observations at single sun position," *Sci. China E, Technol. Sci.*, vol. 43, no. S1, pp. 9–16, Dec. 2000.
[67] X. Li and A. H. Strahler, "Geometric-optical bidirectional reflectance modeling of the discrete crown vegetation canopy: Effect of crown shape and mutual shadowing," *IEEE Trans. Geosci. Remote Sens.*, vol. 30, no. 2, pp. 276–292, Mar. 1992, doi: 10.1109/36.134078.
[68] J. L. Monteith and J. Ross, "The radiation regime and architecture of plant stands," *J. Ecology*, vol. 71, no. 1, p. 344, 1981, doi: 10.1007/978-94-009-8647-3.
[69] Y. Dong *et al.*, "Assessment of the hotspot effect for the PROSAIL model with POLDER hotspot observations based on the hotspot-enhanced kernel-driven BRDF model," *IEEE Trans. Geosci. Remote Sens.*, vol. 57, no. 10, pp. 8048–8064, Oct. 2019, doi: 10.1109/TGRS.2019.2917923.
[70] F. Gao, X. Li, A. Strahler, and C. Schaaf, "Evaluation of the li transit kernel for BRDF modeling," *Remote Sens. Rev.*, vol. 19, nos. 1–4, pp. 205–224, Dec. 2000, doi: 10.1080/02757250009532419.
[71] Z. Jiao, M. J. Hill, C. B. Schaaf, H. Zhang, Z. Wang, and X. Li, "An anisotropic flat index (AFX) to derive BRDF archetypes from MODIS," *Remote Sens. Environ.*, vol. 141, pp. 168–187, Feb. 2014, doi: 10.1016/j.rse.2013.10.017.
[72] F. M. Bréon, F. Maignan, M. Leroy, and I. Grant, "Analysis of hot spot directional signatures measured from space," *J. Geophys. Res., Atmos.*, vol. 107, no. D16, pp. AAC 1-1–AAC 1-15, Aug. 2002, doi: 10.1029/2001JD001094.
[73] T. He, S. Liang, D. Wang, Y. Cao, and M. Feng, "Evaluating land surface albedo estimation from Landsat MSS, TM, ETM+, and OLI data based on the unified direct estimation approach," *Remote Sens. Environ.*, vol. 204, pp. 181–196, Jan. 2018, doi: 10.1016/j.rse.2017.10.031.
[74] S. Liang, "Narrowband to broadband conversions of land surface albedo I: Algorithms," *Remote Sens. Environ.*, vol. 76, no. 2, pp. 213–238, May 2001, doi: 10.1016/S0034-4257(00)00205-4.
[75] M. J. Hill, C. Averill, Z. Jiao, C. B. Schaaf, and J. D. Armston, "Relationship of MISR RPV parameters and MODIS BRDF shape indicators to surface vegetation patterns in an Australian tropical savanna," *Can. J. Remote Sens.*, vol. 34, no. 2, pp. S247–S267, Nov. 2008, doi: 10.5589/m08-042.

Yaxuan Chang received the B.S. degree in geographic information science from Northeast Forest University, Harbin, China, in 2017, and the M.S. degree in geographic information science from Beijing Normal University, Beijing, China, in 2020.

Currently, she is a Staff Member of Tianjin Municipal Bureau of Planning and Natural Resources. Her research interests include the kernel-driven model and the calibration of hotspot parameters of these models based on bidirectional reflectance distribution function (BRDF) data and radiative transfer theory.

Ziti Jiao received the B.Sc. degree in mining engineering from the Wuhan Institute of Technology, Hubei, China, in 1993, the M.Sc. degree from the School of Geography, Beijing Normal University (BNU), Beijing, China, in 2002, the Ph.D. degree in geographic information systems from BNU in 2008, and the Ph.D. degree in remote sensing from Boston University (BU), Boston, MA, USA, in 2009.

He attended the exchange program between BNU and Boston University (BU) in 2004. He is also an Associate Professor with the Faculty of Geographical Science, Institute of Remote Sensing Science and Engineering, BNU. His research interests mainly include modeling reflectance anisotropy and albedo using remotely sensed data to monitor the reflectance characteristics of various land surfaces. More recently, he has been focusing on the development of the kernel-driven bidirectional reflectance distribution function (BRDF) models, including modeling the hotspot effect and snow scattering optics in the kernel-driven BRDF model framework. He is now working on the development of the operational clumping index (CI) products to monitor the Earth's environments using multiangle signatures.

Dr. Jiao is an Editorial Board Member of *Remote Sensing*. He also serves as a Reviewer for *Remote Sensing of Environment* and the IEEE TRANSACTIONS ON GEOSCIENCE AND REMOTE SENSING.

Xiaoning Zhang received the B.E. degree in surveying and mapping from the China University of Mining and Technology, Beijing, China, in 2014 and the Ph.D. degree in cartography and geography information systems from the Faculty of Geographical Science, Beijing Normal University, Beijing, in 2019.

Currently, she is a Post-Doctoral Researcher with Beijing Normal University. Her research interests include albedo retrieving and validation, scale effects of bidirectional reflectance distribution function (BRDF), and the quantitative inversion of vegetation parameters based on BRDF data and radiative transfer theory.

Linlu Mei received the B.S. degree in geographic information system from the China University of Geosciences, Wuhan, China, in 2008, and the Ph.D. degree in atmospheric remote sensing from the Institute of Remote Sensing and Digital Earth, Chinese Academy of Sciences (CAS), Beijing, China, under the Joint Doctoral Training Program between the University of Bremen, Bremen, Germany, and CAS, in 2013.

He is a Senior Researcher with the Institute of Environmental Physics and Remote Sensing, University of Bremen. He is the Leading Developer of the eXtensible Bremen Aerosol/cloud and surfacE Retrieval (XBAER) Algorithm that can be used to derive atmospheric (aerosol and cloud) and surface properties globally. He has authored more than 40 peer-reviewed articles. He has 663 citations and an H-index of 15 (source: Google Scholar). His research interests include radiative transfer theory, aerosol/cloud/surface retrieval, long-term satellite product creation, regional air quality monitoring, and long-term trend analysis.

Yadong Dong received the B.S., M.S., and Ph.D. degrees in cartography and geography information systems from the School of Geography, Beijing Normal University, Beijing, China, in 2011, 2014, and 2017, respectively.

He is currently a Researcher with the Institute of Remote Sensing and Digital Earth, Chinese Academy of Sciences, Beijing. His research interests include the improvement of the kernel-driven model and its application in estimating the clumping index.

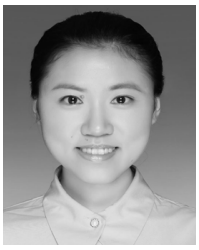

Siyang Yin received the M.E. degree in surveying and mapping engineering from the Institute of Remote Sensing and Digital Earth, Chinese Academy of Sciences, Beijing, China, in 2017. She is pursuing the Ph.D. degree with Beijing Normal University, Beijing.

Her research interests include production and analysis of clumping index data and representative assessment of field data.

Lei Cui received the B.S. degree from the Xiamen University of Technology, Xiamen, China, in 2014. He is pursuing the Ph.D. degree with Beijing Normal University, Beijing, China.

His research interests include inversion of vegetation structure parameters based on waveform LiDAR data and multiangle remote sensing data.

Anxin Ding received the B.S. degree from the Anhui University of Science and Technology, Anhui, China, in 2016, and the M.S. degree from Beijing Normal University, Beijing, China, in 2019. He is pursuing the Ph.D. degree with Wuhan University, Wuhan, China.

His research interests include the RossThick-LiSparseReciprocal (RTLSR) model, the snow bidirectional reflectance distribution function (BRDF) model, and snow albedo.

Jing Guo (Member, IEEE) received the B.S. degree in geographic information science from Northeast Forestry University, Harbin, China, in 2018. She is pursuing the master's degree with Beijing Normal University, Beijing, China.

Her research interests include the kernel-driven model and snow bidirectional reflectance distribution function (BRDF) model.

Rui Xie received the B.S. degree from the Shandong University of Science and Technology, Qingdao, China, in 2018. She is pursuing the master's degree with Beijing Normal University, Beijing, China.

Her research interests include the analysis and statistics of clumping index (CI) products.

Zidong Zhu received the B.E. degree from the Faculty of Geographical Science, Beijing Normal University, Beijing, China, in 2019, where he is pursuing the master's degree.

His research interests include the analysis and statistics of clumping index (CI) products.

Sijie Li received the B.S. degree in geographic information science from Henan University, Kaifeng, China, in 2019. She is pursuing the master's degree with Beijing Normal University, Beijing, China.

Her research interests include the spatiotemporal distribution of gross primary productivity (GPP) and the relationships of GPP and the clumping index (CI).